Journal of Controlled Release 368 (2024) 115–130

Contents lists available at ScienceDirect

Journal of Controlled Release

journal homepage: www.elsevier.com/locate/jconrel

Multi-material 3D printed eutectogel microneedle patches integrated with fast customization and tunable drug delivery

Huan Liu, Xinmeng Zhou, Aminov Nail, Hao Yu, Zilian Yu, Yue Sun, Kun Wang, Nanbin Bao, Decheng Meng, Liran Zhu, Huanjun Li *

Key Laboratory of Cluster Science of Ministry of Education, Key Laboratory of Medical Molecule Science and Pharmaceutics Engineering of Ministry of Industry and Information Technology, School of Chemistry and Chemical Engineering, Beijing Institute of Technology, Beijing 100081, China

ARTICLE INFO

Keywords:
Eutectogel
3D printing
Microneedles
Multi-material
Transdermal drug delivery

ABSTRACT

Microneedle patches are emerging multifunctional platforms for transdermal diagnostics and drug delivery. However, it still remains challenging to develop smart microneedles integrated with customization, sensing, detection and drug delivery by 3D printing strategy. Here, we present an innovative but facile strategy to rationally design and fabricate multifunctional eutectogel microneedle (EMN) patches *via* multi-material 3D printing. Polymerizable deep eutectic solvents (PDES) were selected as printing inks for rapid one-step fabrication of 3D printing functional EMN patches due to fast photopolymerization rate and ultrahigh drug solubility. Moreover, stretchable EMN patches incorporating rigid needles and flexible backing layers were easily realized by changing PDES compositions of multi-material 3D printing. Meanwhile, we developed multifunctional smart multi-material EMN patches capable of performing wireless monitoring of body movements, painless colorimetric glucose detection, and controlled transdermal drug delivery. Thus, such multi-material EMN system could provide an effective platform for the painless diagnosis, detection, and therapy of a variety of diseases.

1. Introduction

Microneedle (MN) patches have emerged as an effective smart monitor and transdermal drug delivery system that can surmount the inherent barriers to drugs or biomarkers uptake across the skin without external energy sources or complex systems [1–4]. The manufacturing of conventional MNs involves micromachining, micromoulding, lithography, and etching, but their complexity and time-consuming process (> 24 h) hinder their customizability, scalability, and financial viability [5–8]. Besides, the need to produce or purchase molds results in additional costs, which is particularly challenging during the research and development stage, where it is essential to fabricate prototypes for analyzing and optimizing the geometric parameters (shape, tip diameter, length, aspect ratio et al.) of MNs [9].

One notable advancement in recent years has been the utilization of high-fidelity digital light processing (DLP) photocurable 3D printing for MN preparation, effectively overcoming challenges related to low precision and poor preparation reproducibility [10–15]. Furthermore, 3D printing has the potential to provide different composite materials to create customized multi-functional objects for individual patients [16]. The MN 3D printing ink is usually formed by integrating photosensitive polymers and active pharmaceutical ingredients (API) [17–21]. However, current MN photocurable ink primarily utilizes water as the solvent, posing difficulties in insoluble and large molecule drugs (accounting for 40% of the developed drug quantity) [22,23]. In addition, its slow photopolymerization rate and limited components also hinder the possibility of 3D printing multi-functional MN on large scales.

Promisingly, deep eutectic solvent (DES) based on the combination of hydrogen bond acceptors (HBA) and hydrogen bond donors (HBD) have recently merged as an effective tool for improving drug solubility and bioavailability [24]. Several approaches, including the integration of DES containing APIs in polymeric systems to enhance drug solubility, are currently undergoing preclinical and clinical evaluation [25,26]. One notable development is the use of polymerizable DES (PDES), which employs polymeric monomers as HBDs and facilitates accelerated polymerization through hydrogen bonding [27–30]. PDES has been utilized in the development of 3D photocurable ink for customizing eutectogels with high elastic modulus (max = 14.2 GPa) or stretchability (max = 3645%) 21–23. Therefore, PDES can be directly transformed into multifunctional eutectogel by photopolymerization [31,32],

* Corresponding author.
E-mail address: lihj@bit.edu.cn (H. Li).

https://doi.org/10.1016/j.jconrel.2024.02.023
Received 11 December 2023; Received in revised form 21 January 2024; Accepted 14 February 2024
Available online 21 February 2024

showing the potential for fast 3D printing of MNs by eliminating drying processes. However, the use of PDES as photocurable ink for direct 3D printing fabrication of multifunctional smart MN patches remains unexplored.

Here, we present novel photocurable inks based on PDES for fast multi-material 3D printing of eutectogel MNs (EMNs) for smart monitoring, colorimetric detection, and subcutaneous drug delivery (Fig. 1). The PDES, a kind of water-free green solvent with ultrahigh solubility for various hydrophobic drugs, is composed of three components including choline chloride (ChCl), 2-hydroxyethyl methacrylate (HEMA), and either itaconic acid (IA) or glycerol (Gly). Fast photopolymerization of the PDES is achieved owing to the synergy of strong hydrogen bond interactions among different components [30], which creates new opportunities for 3D printing fabrication of multi-scale, multi-material, and multifunctional structures. Benefiting from this feature, the stretchable EMN patches, consisting of a soft backing layer fabricated by ChCl/HEMA/Gly-type PDES and rigid needles by ChCl/HEMA/IA-type PDES, was demonstrated by using digital light processing (DLP) 3D printing strategy. Furthermore, such multi-material 3D-printed eutectogels were utilized to rapidly customize multifunctional smart EMN patches integrated with wireless monitoring of human motions, colorimetric glucose detection, and on-demand drug delivery. To the best of our knowledge, this is the first report on the multi-material 3D printing of EMN patches by using PDES. This innovative approach enables the facile customization of EMN patches with diverse functions for personalized medicine.

2. Results

2.1. Design and fast gelation of high drug-loaded eutectogel

Currently, MNs are commonly fabricated through negative molding or 3D printing techniques utilizing hydrogels [33,34]. However, these methods suffer from limited drug loading capacity, time-consuming process, and complex manufacturing [35]. The emerging PDES offer a pivotal strategy to overcome this challenge (Fig. 2a). Three kinds of PDESs were prepared by adjusting the ratio of different components containing ChCl, HEMA, and either IA or Gly (Table S1) in a water bath at 80 °C (Fig. 2b). Then the DES mixture with the crosslinker (0.1% *w*/w) and the photoinitiator (0.1% w/w) was rapidly polymerized under ultraviolet light in 10 s (Fig. S1). The prepared eutectogel was named $C_xH_yI_z$ or $C_xH_yG_z$ (where x represents the molar ratio of ChCl; y represents the molar ratio of HEMA; z represents the molar ratio of IA or Gly). CHI eutectogel can spontaneously form a self-crosslinking network through the strong interaction of hydroxyl groups between PHEMA polymer chains [36]. Therefore, only a small amount of additional crosslinker was necessary to ensure the water swellability of CHI eutectogel. The content of residual monomers in the eutectogel was determined by HPLC (Fig. S2-S4) to detect the polymerization degree of the samples.

The key parameters of the UV polymerization process are shown in Fig. 2c. The results show that the DES has a fast initiation time (10 s), achieving a polymerization degree of 91.48% and quick saturation with

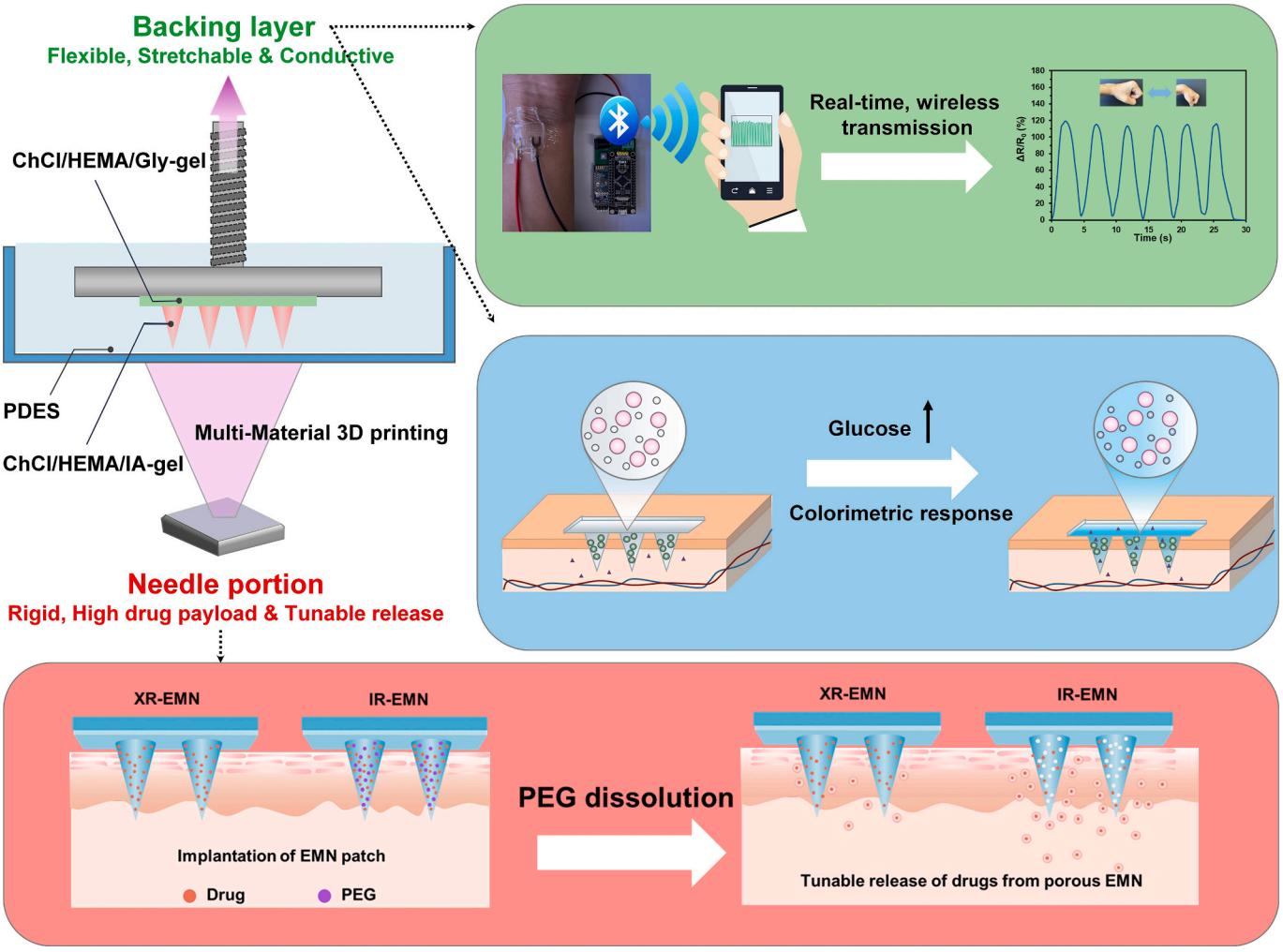

Fig. 1. Schematic diagram of the multi-material and multifunctional 3D printed EMN patches.

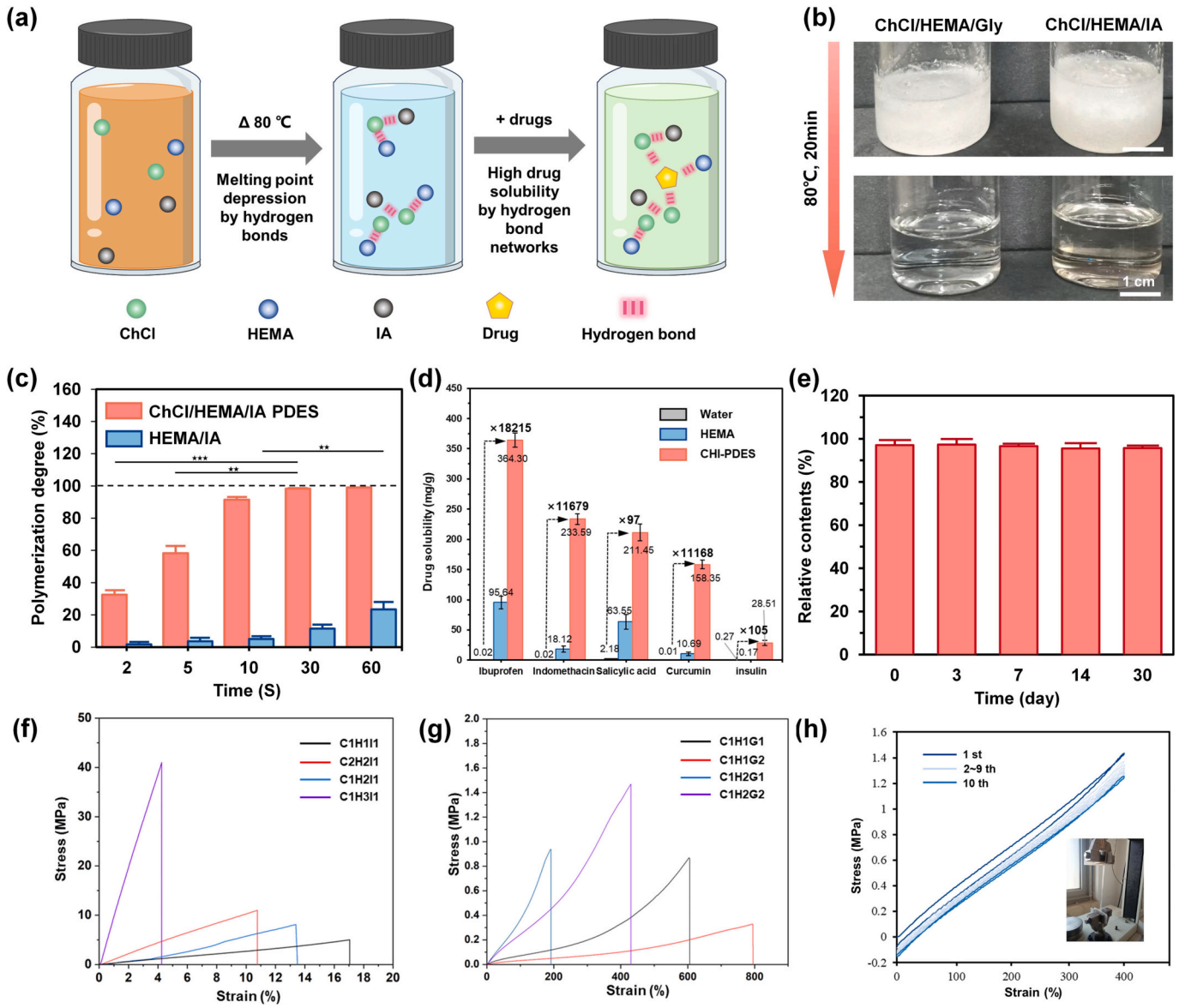

Fig. 2. Multi-functional eutecogel integrated with a stretchable backing layer and rigid needles. (a) Schematic illustration of drug-loaded PDES. (b) Preparation process of PDES. (c) Time-dependent polymerization degree curve of PDES under 405 nm light ($n = 3$). (d) The solubility of APIs in water, HEMA and CHI-PDES (n = 3). (e) Influence of eutectogel on insulin stability (n = 3). (f) Stress–strain curves of the tensile test for the CHI eutectogel with different proportions of monomer. (g) Stress–strain curves of the tensile test for the CHG eutectogel with different proportions of monomer. (h) Cyclic stress–strain curves of the tensile test for the CHG eutectogel.

increasing time. In opposite to DES, the conventional precursor containing HEMA and IA showed low polymerization behavior, and the polymerization degree was only 27.12% within 60 s. The synergistic hydrogen bond interaction among HEMA, IA, and ChCl molecules in the system significantly reduces the induction period of free radical polymerization and enhances the photopolymerization rate [30,37]. These interactions may result in the formation of supramolecular structures, promoting polymerization through ordered aggregates formed by monomers. Quaternary ammonium salts can form hydrogen bonds with protic compounds such as carboxylic acids, similar to some metal salts (*e.g.*, $ZnCl_2$) or ionic liquids, thus it is plausible to speculate that both carboxylic monomer complexes and growing macroradical complexes formed in DESs might exhibit higher reactivity than non-associated species [28]. Additionally, DES can decrease the rate constant of polymerization termination due to increased solution viscosity, similar to observations in ionic liquid-mediated radical-free polymerization [30]. Overall, the abundance of hydrogen bonds in PDES can lower the activation energy of the photopolymerization reaction, accelerating the photopolymerization rate and enhancing double bond conversion. These interactions play a crucial role in facilitating fast 3D printing process.

We further investigated the solubility of a variety of hydrophobic drugs including ibuprofen, indomethacin, salicylic acid, curcumin and insulin in the PDES, as illustrated in Fig. 2d. In some cases, the maximum absorbance of these compounds was shifted (Fig. S5), due to the strong interaction between model drugs and PDES. It should be noted that all investigated experiments show a similar solubility profile, wherein the drug solubility exhibited a significant increase in ChCl/HEMA/IA-type PDES (CHI-PDES) compared to pure water and HEMA. Notably, the solubility of four hydrophobic drugs in HEMA was higher than that in water, but CHI-PDES further increased their solubility (Fig. 2d). There was >18,215-, 11,679-, 97-, 11,168-, and 105-fold enhancement in solubility in CHI-PDES as compare with water for ibuprofen, indomethacin, salicylic acid, curcumin and insulin, respectively at 25 °C.

It was reported that several APIs could not completely dissolve to

form true solution, but instead dispersed in DES as colloidal systems exhibiting the Tyndall effect over a wide concentration range [38]. Investigating the dissolution state of hydrophobic drugs in PDES is crucial for understanding their interaction with solvents. To examine this, clear solutions obtained after centrifugation and filtration were subjected to laser irradiation (Fig. S6). The presence of the Tyndall phenomenon suggests that some APIs in DES may exist as colloids. However, when the laser was directed through both the control group (0.1% starch sol) and DES samples containing APIs, no light beam was observed for any API in DES; only the control group exhibited Tyndall scattering phenomenon. Additionally, dynamic light scattering (DLS) analysis revealed colloidal particles ranging from 50 to 1200 nm present in 0.1% starch sol but no particles (*i.e.*, particle size of zero) were detected in DES with APIs (Fig. S6b). This result was consistent with Tyndall scattering phenomenon observed above. Therefore, these hydrophobic drugs can be effectively dissolved rather than as colloidal particles within CHI-PDES. The substantial drug solubility in CHI-PDES underscores its role as a potent solubilizing agent, a characteristic shared by numerous other pharmaceutical compounds. The observed solubility levels of these drugs in the examined PDESs may stem from various interactions between the solute and solvent such as hydrogen bonds, van der Waals forces, ion-dipole attractions, and dipole-dipole interactions, collectively contributing to effective solubilization of hydrophobic drugs within the solvent medium [18]. The investigated drugs at the atomic level demonstrate the capacity to serve as either HBDs or HBAs (Fig. S7), thus facilitating the formation of hydrogen bonds with PDESs. The substantial drug solubility in CHI-PDES underscores its role as a potent solubilizing agent, a characteristic shared by numerous other pharmaceutical compounds. The observed solubility levels of these drugs in the examined PDESs may stem from interactions between the solute and solvent. These interactions encompass hydrogen bonds, van der Waals forces, ion-dipole attractions, and dipole-dipole interactions between the solute and solvent, collectively contributing to the effective solubilization of hydrophobic drugs within the solvent medium [18]. The investigated drugs at the atomic level demonstrate the capacity to serve as either HBDs or HBAs (Fig. S7), thus facilitating the formation of hydrogen bonds with PDESs.

Furthermore, the structural stability of four hydrophobic APIs and insulin after the photopolymerization of PDES was verified by UV spectra and circular dichroism (CD) spectra (Fig. S5), respectively. The absorption peaks in the UV spectra for the four hydrophobic APIs and the CD spectra for insulin were almost unchanged, indicating that their structures remain stable during the photopolymerization of PDES. The contents of APIs after photopolymerization were over 90% (Fig. S8), demonstrating a slight loss of APIs during the process. The long-term stability of insulin in the prepared eutectogel was further verified by HPLC (Fig. S9-S10). The results revealed that the drug content remained almost unchanged for 30 days, accompanied by a 1.44 ± 0.02% insulin reduction rate (Fig. 2e). These findings indicate that CHI-PDES possesses remarkable drug loading capacity and stability, which is crucial for designing MN patches that require high drug loading.

In order to achieve rapid 3D printing multi-material EMNs, a high photopolymerization rate of the printing ink is essential, which is significantly influenced by the photoinitiator [39,40]. Therefore, the maximum absorption wavelength of three different photoinitiators was first examined using UV–visible spectrophotometer (Fig. S11). The results revealed that ethyl phenyl (2,4,6-trimethylbenzoyl) phosphinate (TPO-L) had a maximum absorption wavelength closer to the working wavelength of DLP printer (405 nm), making it the ideal choice for DLP 3D printing eutectogel. The mechanical properties of 3D-printed structures play a pivotal role in determining their suitability for various applications. For the fabrication of needle portion, the rigidity of printed constructions is an important factor for skin penetration. To explore these aspects, the mechanical properties of the CHI-gel were investigated through a tensile test. As shown in Fig. 2f, the CHI-gel fabricated using three different monomer ratios exhibited high rigidity. The ultimate tensile strength slightly increased by decreasing ChCl content. C1H3I1 exhibited the highest value of 41.8 MPa with the optimal Young's modulus (1.2 GPa), indicating the highest rigidity among all the samples. In contrast, the tensile strain of soft C1H2G2 as the backing layer is up to 428%, and the tensile stress is ~1.5 MPa (Fig. 2g). It is highly stretchable and maintains sufficient toughness during the cyclic tensile test (Fig. 2h). The material of backing layer exhibited high stretchability and strength, making it highly flexible in its deformation and suitable for application to various parts of the human body's skin.

The peak intensity can reflect the extent of the polymerization reaction at 1652 cm^{-1} associated with the C═C bond in FTIR spectrum (Fig. S12). As the photopolymerization occurs, the peak intensity at 1652 cm^{-1} decreases correspondingly, further indicative of a high degree of polymerization. In addition, the peaks observed at 1728 cm^{-1} in the DES is attributed to −COOH of IA and HEMA. After polymerization, these peaks shifted to lower wavenumbers (1705 cm^{-1}). A similar phenomenon is also observed in the FTIR spectrum of the CHG-gel used as the backing layer (Fig. S13). The XRD results (Fig. S14-S15) of the two eutectogels exhibited broad diffraction peaks at $2\theta \approx 22^{\circ}$, indicating their amorphous structure [27]. The glass transition temperature (Tg) of the needle portion eutectogels was detected at 80.7 °C and 33.3 °C in the DSC spectrum (Fig. S16), both of which were higher than room temperature, indicating that the needle portion eutectogel could maintain high hardness at room temperature. Conversely, the DSC spectrum (Fig. S17) of the backing layer eutectogel showed a Tg of −31.3 °C, indicating its flexible characteristics. The thermogravimetric analysis (TGA) of the needle portion eutectogel decomposed at approximately 220 °C, while the backing layer eutectogel decomposed at around 180 °C, indicating excellent thermal stability (Fig. S18-S19). Additionally, the eutectogels exhibited conductivity (Table S2) and can function as a flexible conductor to maintain lamp brightness (Fig. S20). The backing layer eutectogel showed better conductivity (61.42 mS/cm) than conventional hydrogel materials [30–32], indicating its potential for use in wearable sensors or electrical stimulation response release.

2.2. Multi-material 3D printing customized EMN patches

As a type of 3D printing MNs inks, the design of PDES needs to ensure sufficient biocompatibility after polymerization. In this study, a typical choline chloride-based DES was used for the formulation of PDES. Choline chloride, a commonly used food additive, was selected as HBA [24]. HEMA is a kind of photocurable material that can be polymerized by free radical reaction of the acrylate group. PHEMA exhibits good biocompatibility and finds wide applications in soft contact lens materials, dentistry and tissue engineering [36]. IA is a well-known bio-based unsaturated organic acid produced industrially from glucose by fermentation [41]. Hydrogels by synthesized by IA polymerization are non-toxic and have been extensively studied for pH-sensitive microgels in anti-tumor medication release [42]. Theoretically, the CHI eutectogel prepared in this study demonstrates good biocompatibility and holds potential for *in vivo* drug delivery. Although MN patches typically feature a rigid needle portion, however, the design of the backing layer is often overlooked due to the complexity of the preparation process [33]. Impressively, for our PDES as photocurable ink, hierarchical DLP 3D printing could be applied for separate production of MN backing layer and MN needle portion, providing them with distinct structural and functional characteristics (Fig. 3a). In this process, the green fluorescent substances and the red one were added to the PDES for MN backing layer and another PDES for MN needle portion, respectively. Then the EMN was prepared by hierarchical 3D printing. Finally, the EMN combined with a green backing layer and red needle portion was observed under the fluorescence microscope (Fig. 3b).

Hierarchical 3D printing allows for the adjustment of print numbers by editing the print models (Fig. 3c), resulting in a high-precision (MN tip diameter < 20 μm) MN patch (Fig. 3d). Additionally, MN patches with different structures (Fig. 3e) can be fabricated by the

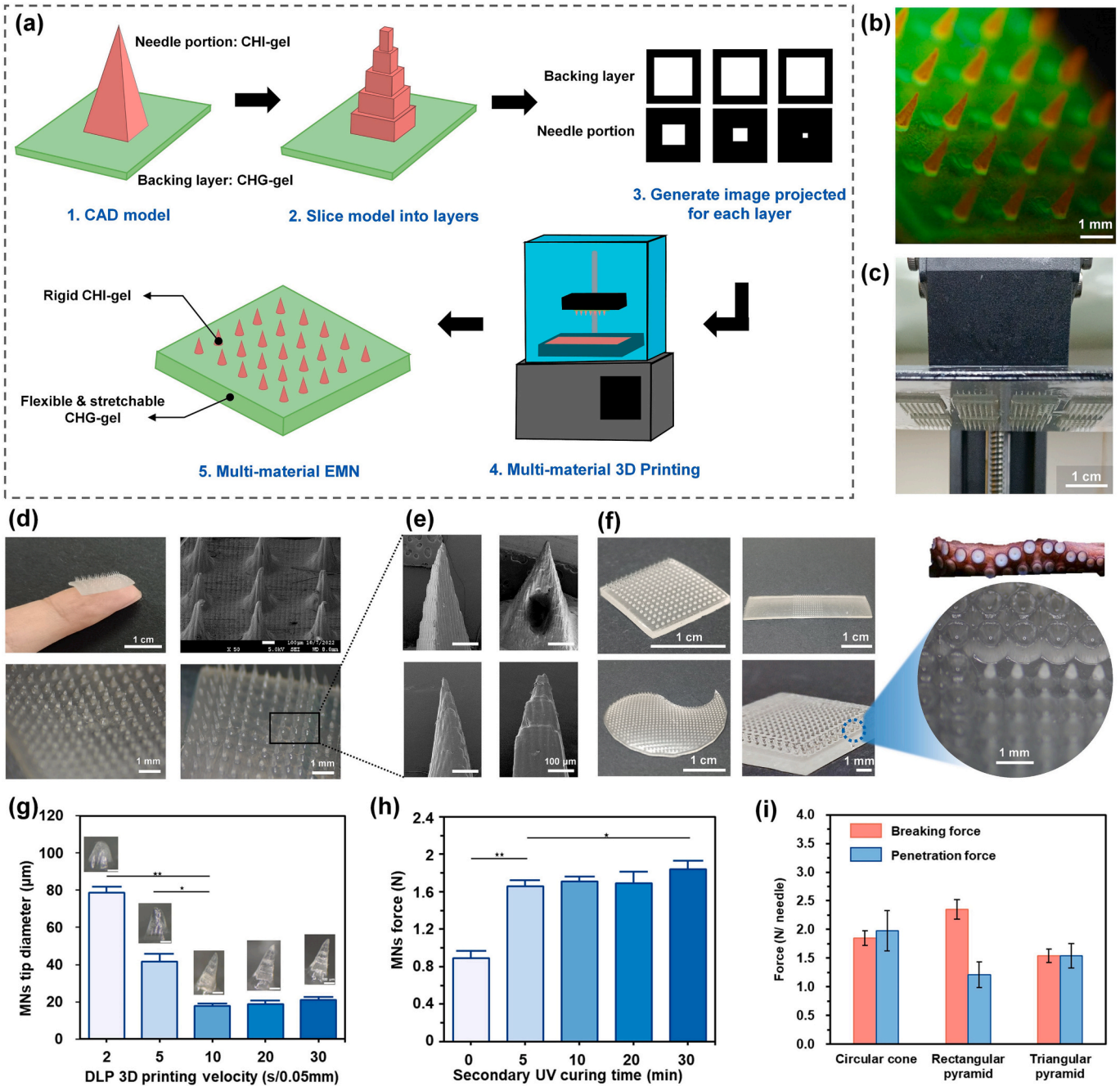

Fig. 3. Multi-material 3D printing of hierarchical EMN patches. (a) Schematic diagram of multi-material 3D printing of hierarchical EMNs. (b) Hierarchical 3D printing of EMNs loaded with different fluorescent substances (green: backing layer, red: needle portion). (c) Batch preparation of EMNs. (d) EMNs of different heights were manufactured by optical microscopy and SEM images. (e) SEM image of EMNs with different shapes. (f) 3D printing EMNs with different structures. (g) EMN mechanical strength by DLP 3D printing with different light exposure times per layer ($n = 3$). (h) EMN mechanical strength by DLP 3D printing with different secondary light exposure times (n = 3). (i) Breaking force and penetration force with different EMN needle shape structures (n = 3). (For interpretation of the references to color in this figure legend, the reader is referred to the web version of this article.)

programmability of 3D printing. Notably, our 3D printing strategy simplifies the preparation process of hollow microneedles, thereby effectively expanding the application potential of EMNs and offer new avenues for personalized manufacturing of MNs. 3D printing technology also allows the preparation of MN patches for different uses, such as conventional patch shape, wound patch shape, eye patch shape, and octopus tentacle structure at the edge of MNs (Fig. 3f), which can enhance their adhesion. This approach makes the one-step production of EMNs combining hard needles and a flexible backing more accessible. The excellent stretchability (Movie 1) can be applied to any part of the human body (Fig. S21). The results demonstrate 3D printing enables the design and manufacture of MNs customized to individual patients and their specific treatment needs, thereby enhancing the adaptability and efficacy of MNs. This represents a powerful tool for achieving personalized medicine.

The MN structure's size depended on the resolution and brightness of the projector used in the DLP 3D printing process [10,11]. The high-fidelity projector used in this study acted as a light source, allowing photo crosslinking at the irradiation feature to produce the gel layer. The illumination time of each layer (0.05 mm) was crucial to the accuracy of

the MN in the DLP 3D printing process. The experimental results (Fig. 3g) showed that prolonging the illumination time of each layer could improve the accuracy of the MN, and the highest accuracy (16 μm) could be achieved at 10 s/layer. In addition, the MN structure design included the backing layer with less precision requirements. Therefore, the rapid manufacturing of the backing layer could also be achieved by increasing the slice thickness (0.5 mm) and shortening the illumination time (5 s). The 3D printing process of the MN could be controlled within 10 min using the hierarchical printing method. Compared to other MN 3D printing processes that usually require >2 or 3 h, this method provided an ultrafast and high-precision MN preparation process. The secondary light curing process was common in DLP photocuring printing technology to polymerize the unreacted polymer monomer in the eutectogel. The experimental results (Fig. 3h) showed that it took only 5

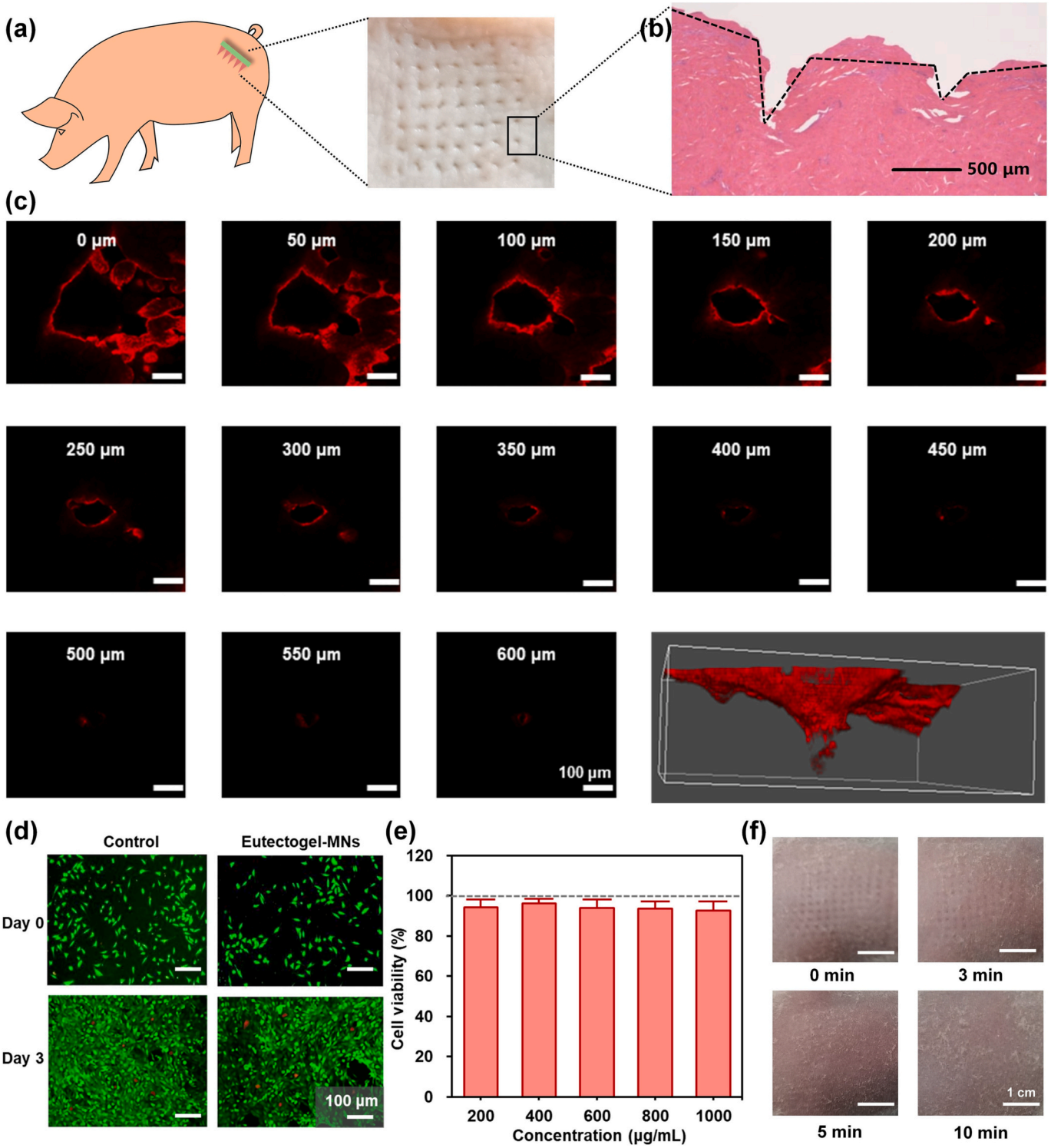

Fig. 4. Characterization of EMN patches. (a) Macroscopic view of EMNs inserted into porcine cadaver skin. (b) HE staining section observation of EMNs inserted into porcine cadaver skin. (c) CLSM observation of EMNs inserted into mice skin. (d) Images of high concentration EMN extraction solution effect on NIH-3 T3 cell growth. (e) Impact of EMN extraction solution on NIH-3 T3 cell viability ($n = 3$). (f) Evaluation of EMNs effect on mice skin irritation and recovery.

min to completely solidify the MN to achieve the mechanical strength (1.68 N/ needle) required to pierce the skin (0.06 N/ needle) [43]. The above experimental results show that high-precision MN patches can be rapid one-step (< 20 min) prepared using 3D printing PDES (Movie 2). The structure and shape of MNs can be easily changed according to the design, and mass production can be achieved. This method solves the problems of time-consuming and low insulin drug loading in conventional MN preparation technology, offering new ideas for the design and preparation of novel MNs.

2.3. Optimizing the structural design of EMNs

The design of microneedle (MN) structures, including shape and aspect ratio, greatly influences their penetration performance [10–15]. Optimal structural designs vary for different MN materials. A finite element analysis (FEA) was established to evaluate the mechanical strength and penetration performance of EMNs, as shown in Fig. S22a. The force-displacement diagram demonstrates the gradual increase in reaction force on the MN with displacement during the quasi-static simulation of MN mechanical strength. Local deformation results in stress concentration below the tip, leading to MN breakage when the Von Mises stress reaches the yield stress (Fig. S22b). The penetration process of MNs into the skin is simulated using a conventional three-layer model (stratum corneum, epidermis, and dermis) (Fig. S22c). The presence of penetration force causes changes in local stress distribution during MN insertion (Fig. S22d). Cracks in the stratum corneum, which may expand and produce tearing, are observed only in this layer due to its significantly higher hardness compared to the dermis. The penetration force is evaluated in the screening of MN structure, with greater mechanical strength and smaller penetration force being desirable (Fig. S23). For MNs, a larger aspect ratio results in a smaller penetration force and easier skin piercing. However, the corresponding mechanical strength is also smaller, making it more prone to breakage [44]. Through simulation and further experiments, the optimal needle shape was determined to be a pyramid MN with a bottom diameter of 300 μm and an aspect ratio of 3:1 (height 900 μm). These geometric parameters exhibit the best mechanical strength and penetration force (Fig. 3i) for practical application. Therefore, these optimized geometric parameters were used to prepare multifunctional EMNs in the subsequent experiments. This experimental simulation method was used to systematically evaluate geometric parameters, providing valuable insights for designing MN structures of different materials. This approach could potentially serve as a reference for future MN material design and optimization.

2.4. Characterization of EMN patches

The MNs with much hardness present more advantages for transdermal drug delivery through the skin [4–6]. Based on the previous mechanical examinations on MNs, further preclinical testing was conducted by administering EMNs on isolated porcine cadaver skin (Fig. 4a). As anticipated, the MN application resulted in an enduring puncture site on the skin surface and a penetrating cavity (~500 μm) in the epidermis (Fig. 4b), thereby verifying the successful penetration and deposition of the MN in the stratum corneum. The discrepancy between the insertion depth and MN length can be attributed to the skin's high viscoelasticity [45].

Rhodamine B (RhB) loaded EMN was prepared to visualize the skin penetration of the drug. Confocal laser scanning microscopy (CLSM) was used to scan the mice's skin layer by layer to evaluate the penetration depth. The images were taken at different depths and the fluorescence is mainly distributed at depths between 0 and 600 μm (Fig. 4c). Continuous fluorescence signals indicate that the drug in MNP diffuses into the skin after insertion. The results of 3D reconstruction showed that the drug distribution was pyramidal. The drug content gradually decreases from the base to the tip, which is related to the pyramid shape of the MN. The results showed that EMN could completely penetrate the epidermis for drug delivery.

In light of the promising mechanical properties, the biocompatibility of EMNs was investigated through cytotoxicity experiments. As shown in Fig. 4d, the fabricated EMNs exhibited negligible cytotoxicity. The NIH-3 T3 cell culture medium was mixed with a high concentration (1 mg/mL) of the EMN patches extract, and the cell activity was comparable to that of the normal culture medium. After 24 h of exposure to varying concentrations of EMN extract, the CCK-8 method was used to determine cell viability, which exceeded 90% (Fig. 4e). To evaluate the effect of micro acupuncture on skin irritation and recovery performance, the EMN was applied to the depilated mice's back skin for 10 min and then removed to observe the EMN insertion into the surrounding skin and recovery. The experimental results (Fig. 4f) indicated that the EMN did not cause skin redness and swelling, further verifying its excellent biocompatibility. The EMN recovered quickly after removal, as observed in human healthy volunteers (Fig. S24). The negligible cytotoxicity and skin irritation of the eutectogel may be attributed to the biocompatibility of the matrix materials (natural materials ChCl and biocompatible poly HEMA-IA) [46–48].

2.5. EMN patches for wireless monitoring of human motions

Continuous stretching of the skin wound may impede the healing process. Especially in diabetic patients, this intense stretching often goes unnoticed due to nerve damage in the foot. Monitoring physical activity during wound healing aims to observe the involuntary and forceful stretching around the wound, particularly at joints. Repeated exercises in these areas hinder the formation of blood vessels, cells, and tissues around the wound, hampering the healing process [30]. Therefore, monitoring movement should also be an essential application in the design of multi-material EMNs. As mentioned earlier, the multi-material EMNs exhibited excellent stretchability and electrical conductivity (Fig. 5a), which is beneficial for their application in strain sensors with a low limit of detection (1%). To demonstrate their potential in flexible health motion sensor, the EMN was affixed to the wrist and connected with the circuit board and smartphone to design a wireless body motion monitor, which received the real-time motion of the body surface on the smartphone *via* Bluetooth (Fig. 5b). As shown in Fig. 5c, the EMN sensor effectively captures electrical signals at both low (50%) and high (200%) strains, and the signal amplitudes increase proportionally with strain. The gauge factor, which represents the sensitivity of the sensor, was calculated to be 1.025 within the strain range of 0–300% (Fig. S25), indicating significant sensitivity and stable, repeatable signals.

Due to its exceptional sensitivity and stability, the EMN can be used as wearable sensors for real-time and accurate detection of human body movements, such as the joint motion of fingers, wrist and neck. When applied to the finger, the bending motion of the finger was precisely recorded (Fig. 5d), where different bending angles were determined by different ionic conductivity signals. Furthermore, the signal strength under different frequencies from slow to rapid remains steady (Fig. 5e), indicating excellent independence on the test frequency. In addition to multi-functional subtle movements, large human movements can also be monitored by targeting this EMN sensor to the wrist (Fig. 5f). Due to the excellent antifreeze and solvent retention capabilities of the EMN sensor, the sensor exhibits consistent response patterns without signal degradation at temperatures ranging from −20 to 60 °C, highlighting its stability under various temperature conditions (Fig. 5g-h). These findings demonstrate the potential of the wireless EMN sensor in applications related to joint disease diagnosis and wound healing monitoring.

2.6. EMN patches for colorimetric glucose detection

Compared to motion sensing, biosensing is more focused on the analysis of biomarkers within the body for disease diagnosis. Interstitial fluid (ISF) within skin tissue resulting from blood transcapillary

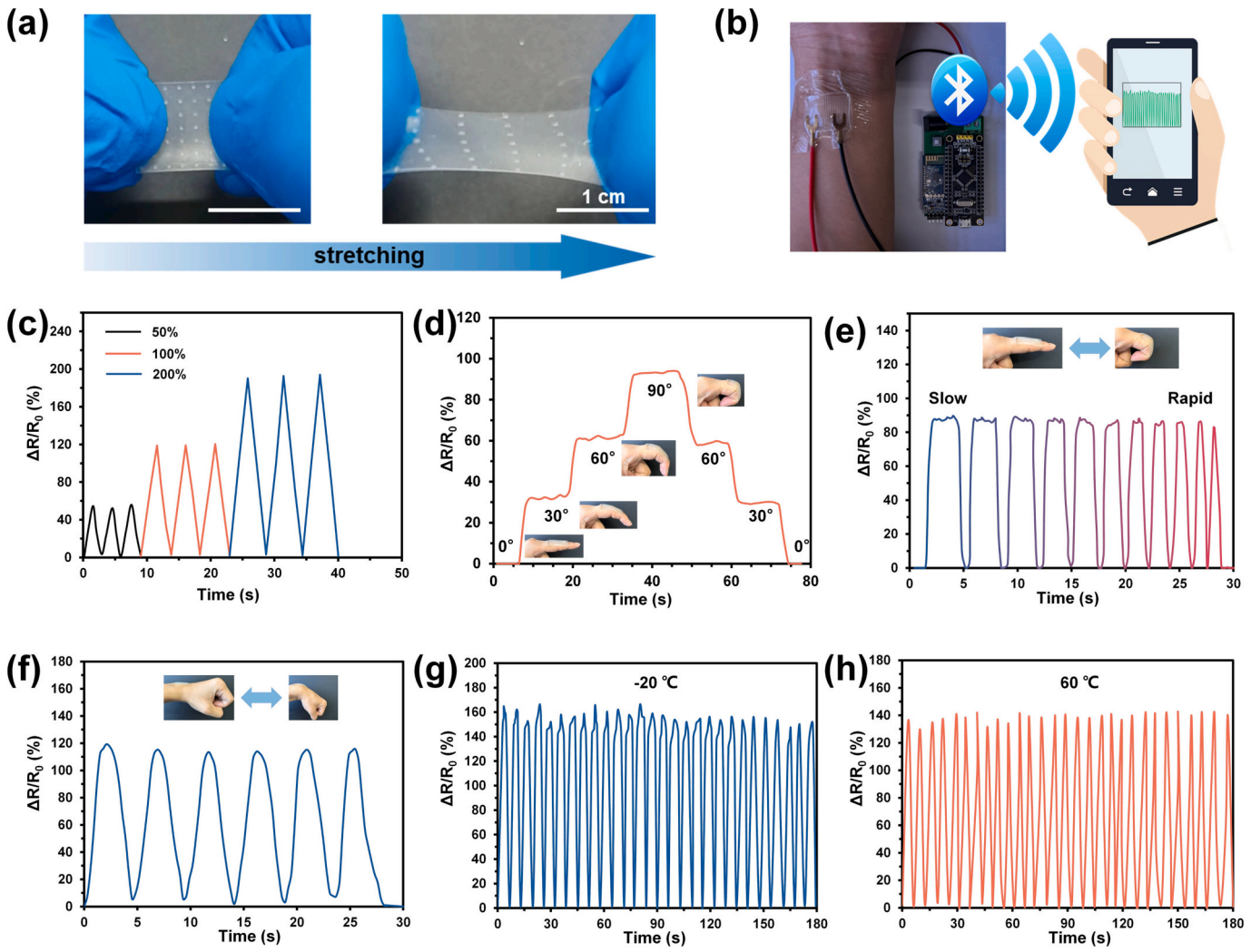

Fig. 5. The motion sensing of multi-functional EMN. (a) Photograph of flexible and stretchable backing layer. (b) Photograph of resistance detection machine using real-time and wireless transmission (c) Resistance variation of the CHG eutectogel sensor responded to the various cyclic tensile strains and bending angle (d). (e) Resistance variation of eutectogel in finger motion at different speeds. (f) Resistance variation of eutectogel in the wrist. Resistance variation under repeated loading and unloading of 100% strain at −20 °C (g) and 60 °C (h).

filtration is an attractive source of biomarkers [1]. To enable the colorimetric analysis of ISF extraction, MNs should be non-dissolvable and exhibit high shellability, and have adequate mechanical strength to facilitate skin penetration as well as high affinity for water to ensure the rapid and substantial absorption of ISF [9]. Although colorimetric MNs can be easily fabricated, these reported methods require a long process and extra devices for operation and analysis. Here CHG-gel contained 3,3′,5,5’-Tetramethylbenzidine (TMB) was adopted as the backing layer material, CHI-gel contained horseradish peroxidase (HRP) and glucose oxidase enzyme (Gox) as the needle portion for colorimetric EMN was prepared by multi-material 3D printing. Upon glucose challenge, Gox selectively catalyzes the extraction of glucose from the MN into gluconic acid and H_2O_2. In the presence of H_2O_2, HRP catalyzes the oxidation of the TMB contained in the backing layer, causing an immediate color change of the sensing layer, with high selectivity (Fig. 6a).

In order to evaluate the color development response of colorimetric EMNs (CEMNs) to glucose, the CEMNs were inserted in 1% agarose gels containing 10 mmol glucose to simulate the *in vivo* skin ISF extraction process. As the insertion time increased, the cyan color became darker and reached the maximum at 10 min (Fig. 6b). The representations of color changes corresponding to glucose concentrations ranging from 0 mmol to 20 mmol can be found in Fig. 6c. The analysis of the color shift was quantified through an RGB histogram analysis. When CEMNs turned cyan in a glucose-dependent manner, the values of all three channels decreased in similar trends. As the red channel showed the steepest change, the red RGB value was employed as a positive indicator correlated with glucose levels. The average response curve (R^2 = 0.9946; Fig. 6d) from several measurements (3 times) was utilized to estimate glucose concentrations in *in vivo* experiments.

Subsequently, the feasibility and performance of the instrument-free *in vivo* skin ISF glucose biosensing using the combination of CEMN and a smartphone were studied in streptozotocin (STZ)-induced diabetic mice. The CEMNs was thumb pressed into the skin of the STZ-induced diabetic mice back for 10 min to ensure adequate extraction of the skin ISF before removal, light color on the CEMN was observed for the mice with normoglycemia (4.3 mmol). Conversely, a cyan color can be observed on the CEMN for the mice with hyperglycemia (16.1 mmol), respectively (Fig. 6e). The results were also compared with those obtained using a glucometer, revealing no significant differences between them (Fig. 6f). This suggests that the combination of CEMNs and a smartphone can attain the same level of accuracy and sensitivity as traditional glucometers, potentially offering painless and straightforward blood glucose level monitoring with enhanced patient compliance. Compared with prior studies of skin ISF glucose detection using MNs [9], the multi-material CEMNs detection system holds the advantage of rapid customization without the need for a centrifugation process or complex

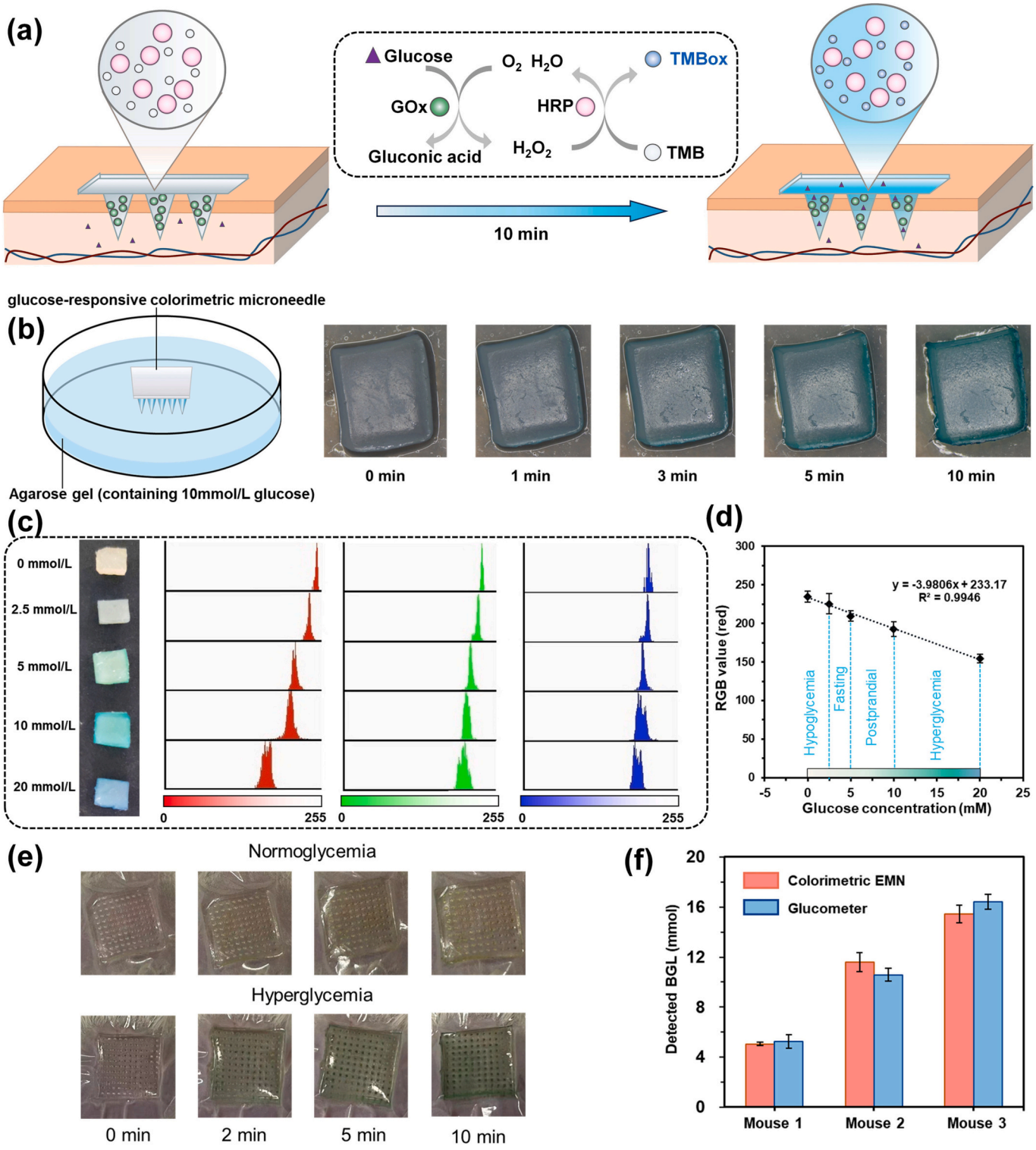

Fig. 6. The biomarker detection of colorimetric EMN. (a) Schematic diagram of the colorimetric EMN. (b) Schematic and snapshots of the colorimetric EMN color change in an agarose-based gel containing 10 mmol glucose solution to mimic the ISF extraction. (c) Left: a scanned image showing the color changes of the transdermal colorimetric patches after glucose (0–20 mmol) extraction from EMN. Right: RGB color histogram of the scanned image, analyzed with ImageJ software. (d) Linear calibration curve between the greyscale values of GBMPs and the glucose concentrations recorded by a smartphone and the inset is corresponding digital photos ($n = 3$). (f) BGLs in 3 mice were measured using a glucometer or colorimetric EMN combined with a smartphone.

analytical instruments.

2.7. Drug-loaded EMN patches for on-demand drug delivery

For BGLs control after BGLs monitoring using CEMN, the insulin-loaded EMN was then applied for painless and syringe-free insulin delivery once the mice were diagnosed as hyperglycemic levels by CEMN. To ensure the effectiveness of transdermal formulations, sustained drug release is essential. Without it, the intelligent release of the drug becomes less relevant [49]. To achieve the sustained release, the increased

drug loading is necessary. However, most existing insulin microneedles suffer from insufficient loading capacity, with an average of only 0.07–3.66 μg/needle [50]. For a MN patch distributed in a 10 × 10 array, the drug load is only 7–366 μg, which is far less than the average human's daily requirement of 0.8–2.0 mg of insulin to maintain blood glucose stability [51–53]. Remarkably, EMN offers a significant advantage in this regard. They boast an impressive loading capacity of insulin (42.81 ± 1.72 μg/needle), which is 26 times higher than that of conventional polymer MN (Fig. 7a) [54–63]. This enables an EMN to contain a sufficient amount of insulin for one day's worth (~ 4.3 mg) within a small area (< 1 cm^2), thereby improving the quality of life of diabetic patients.

Another notable advantage of eutectogels is the ability to adjust drug release kinetics by varying the amount of PEG porogen added to the composition (Fig. 7b). The effect of PEG1500 content on the 3D printing resolution of EMN was initially evaluated. It was observed that PEG1500 with over 50% content would precipitate in CHI-PDES; hence, prescriptions exceeding this threshold were excluded from this experiment. With the increase of PEG1500 content, the polymer monomer content in the 3D printing ink decreases, resulting in longer exposure time for curing. Therefore, it is necessary to extend the printing time for each layer to achieve high-resolution 3D printing with higher PEG1500 contents. Experimental results in shown Fig. S26 demonstrate that the appropriate printing speed for PDES with 20% PEG1500 is 15 s/0.05 mm while for those containing 40% PEG1500, a suitable printing speed is achieved at 20s/0.05 mm. Adequate extension of the printing time enables EMN to maintain its high resolution. Subsequently, the impact of varying amounts of PEG1500 on the mechanical strength of EMN was evaluated through mechanical test (Fig. S27). The results indicates that as the PEG content increases, there is a gradual decrease in the breaking force by EMN samples. The minimum breaking force was observed at 50% PEG1500, but it still falls within an acceptable range (> 0.06 N) [43]. As shown in Fig. S8, skin piercing experiments demonstrate the successful penetration into porcine cadaver skin using EMNs with different PEG contents. The needle tip did not fracture after penetration and only experiencing minimal deformation, which is crucial for ensuring the safe application of microneedles. Despite being a solid at room temperature, PEG1500 possesses a certain level of hardness although its mechanical strength is not as high as CHI eutectogel. Therefore, incorporating a high content of PEG1500 did not compromise its ability to penetrate the skin.

The transdermal release profile of insulin-loaded EMNs in porcine cadaver skin was quantitatively determined using an improved Franz diffusion cell and HPLC (Fig. 7c). Results indicated that in the absence of a PEG porogen, the drug was tightly enclosed within the polymer network structure, leading to an extremely slow-release rate (24 h release rate < 5%). This was not conducive to MN release and could not achieve the desired therapeutic effect. However, the drug release rate significantly improved after adding the porogen. This was because the porogen dissolved after the MNs contacted the skin interstitial fluid, forming holes on the surface of the polymer network structure, thereby accelerating drug dissolution [34,64]. When the porogen content was 40%, the EMNs were almost completely released within 2 h (release rate of 68.75%), after which it entered the release platform period. This immediate-release MN (IR-MN) could be used to inhibit the rapid increase of postprandial blood glucose. Conversely, when the porogen content was 20%, the EMNs were continuously released within 24 h and reached a high release rate (24 h release rate 78.64%). This extend-release MN (XR-MN) could be used to regulate basal blood glucose levels [4,5]. This result was further supported by electron microscopy

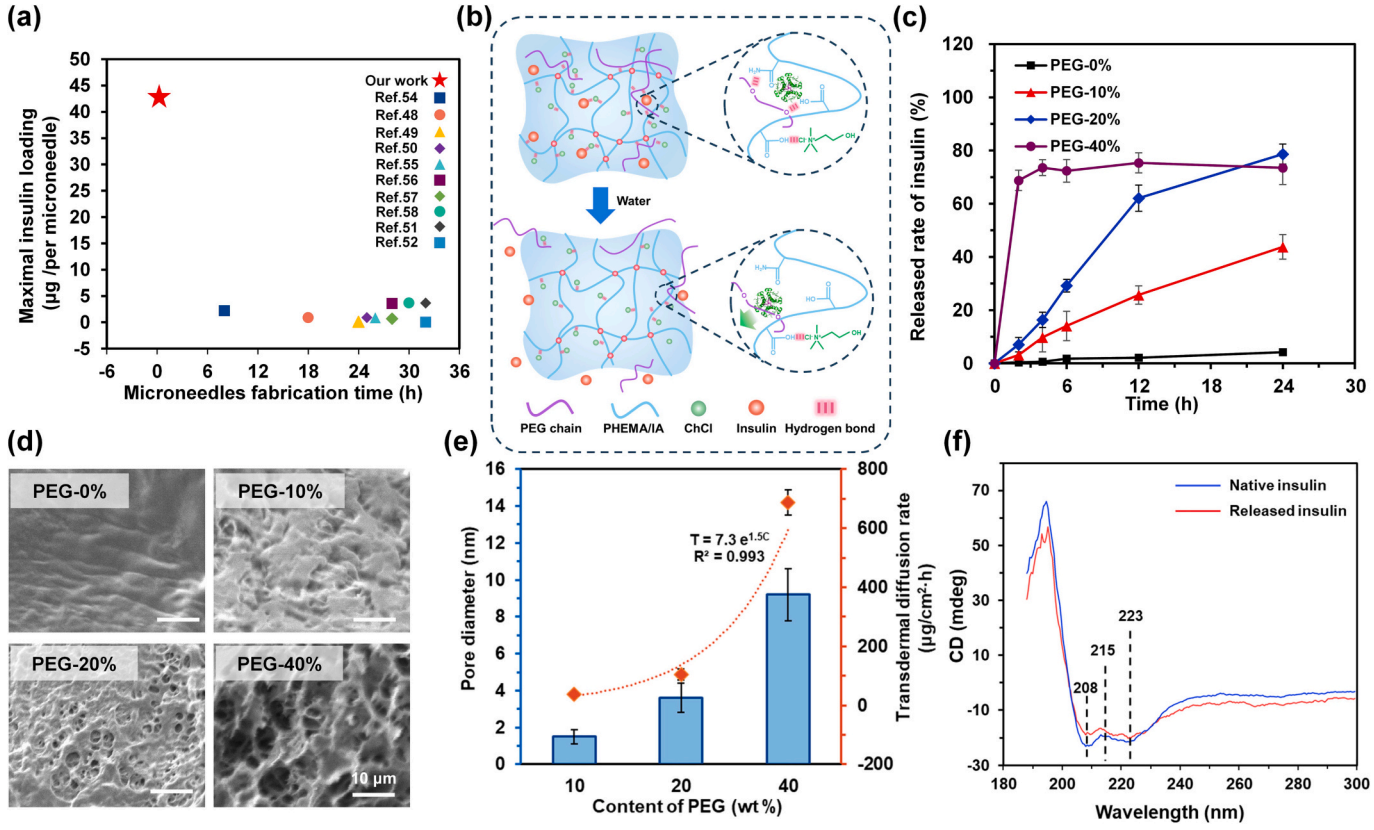

Fig. 7. *In vitro* transdermal behavior with customized insulin release rate. (a) Literature comparison of insulin MNs preparation time and drug loading. (b) Schematic diagram of the regulation for insulin release rate using PEG. (c) Experimental setup for *in vitro* drug release experiment and influence of different contents of porogen on insulin release from MNs *in vitro*. (d) SEM images of EMN surface structure after drug release. (e) Regulation of insulin release rate and pore diameter by the content of PEG. (f) CD chromatogram of insulin before and after EMN release.

observation (Fig. 7d). As the content of porogen increased, more pores were observed on the surface of the MNs after swelling, resulting in faster drug release. Fig. 7e illustrates that this acceleration of insulin release rate increases exponentially with the PEG content, mirroring a similar trend seen in pore diameters. This indicates the potential for customized insulin release by employing the fitted curve (n = 0.993), which aligns with first-order kinetics. To assess the structural stability of insulin before and after release from EMNs, circular dichroism (CD) spectra were employed to evaluate its secondary structure, including alpha helix and beta-sheets [65]. Fig. 7f depicts both curves with peaks at 208 and 215 nm, corresponding to the alpha helix and beta-sheets of insulin, respectively. This observation indicates that insulin maintains its structural stability throughout the release process.

Notably, high drug-loaded EMNs may be susceptible to sudden release due to the potential burst release from the outermost layer during *in vivo* swelling. This phenomenon is unfavorable for achieving sustained drug release and optimal therapeutic efficacy. The sudden release of insulin was not observed due to its low content within EMNs in previous experiments. Ibuprofen, with the highest solubility in PDES (364.3 mg/g), was chosen as a model drug to explore the release profiles of EMNs. With increasing contents of ibuprofen, a sudden release occurs when reaching 200 mg/g (Fig. S29a), resulting in a significantly higher release rate of 50.2% within 1 h compared to the normal rate of 19.5%. To address this challenge, additional crosslinkers were incorporated into PDES to enhance the crosslinking density of eutectogels and suppress abrupt drug releases. Under identical drug loading conditions (300 mg/g), an increase in crosslinker content effectively inhibits the occurrence of sudden releases (Fig.S29b). Furthermore, augmenting crosslinker content leads to a rapid reduction in drug release rate, providing valuable insights for future development towards long-acting controlled-release EMNs. Therefore, comprehensive pre-clinical research is crucial for addressing potential risks associated with sudden drug releases when dealing with different drugs. Furthermore, the drug release process of EMNs was detected using an *in vivo* imaging system (Fig. 8a). Compared with XR-MN, the fluorescence signal of the IR-MN penetrating site was >5 times stronger in the first 2 h, and the fluorescence model was stronger with higher porogen content (Fig. 8b). This further verified that the system could achieve drug delivery with porogen content control. These findings suggest that the use of 3D printing EMNs could provide a promising approach for personalized medicine, allowing for tailored drug delivery based on individual needs.

Streptozotocin (STZ) induced diabetic mice were treated with different administration methods to verify the therapeutic effect of insulin-loaded EMN [5]. The insulin dose in each EMN patch was controlled at 50 μIU with different porogen content. Next, The EMN patch was applied to the back epidermis of the depilated mice and fixed with surgical tape. Blood glucose was measured at regular intervals using a commercial blood glucose meter. The experimental results (Fig. 8c) showed that the effectiveness of different EMN patches on real-time insulin release was directly reflected in the hypoglycemic effect.

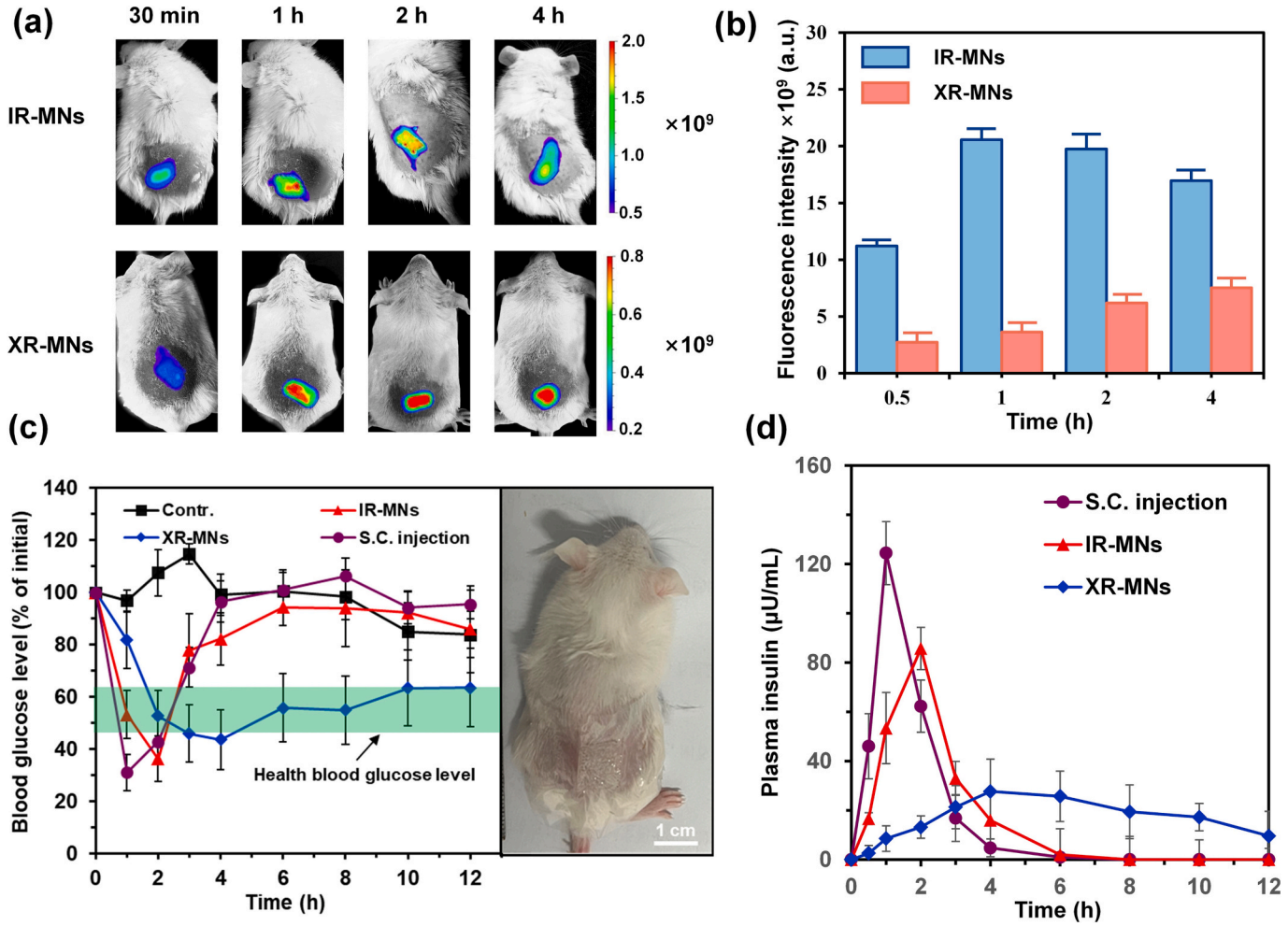

Fig. 8. *In vivo* treatment of diabetes using EMNS with different insulin release rates. (a) Fluorescence image of the skin site treated with EMNs loaded with a fluorescent substance. (b) Fluorescence intensity-time curve (n = 4). (c) Influence of various insulin treatment methods on blood glucose levels in diabetic mice (n = 8). (d) Impact of various insulin treatment methods on plasma insulin concentration in rats (n = 8).

The prepared insulin-loaded EMN patch significantly affected diabetes, as demonstrated by satisfactory blood glucose control.

Mice treated with subcutaneous injection of conventional insulin and IR-MN resulted in a ~ 70% decrease in blood glucose within 1–2 h, followed by a rapid return to the initial level within 4 h. In contrast, glucose levels administered by XR-MN mildly decreased and maintained long-term normal blood glucose. The controlled release characteristics of EMN are entirely due to the blocking effect of crosslinked polymer matrix and porogen. The data showed that changing the matrix material can adjust the insulin release kinetics. IR-MN can rapidly reduce blood glucose levels like subcutaneous injection of insulin, while XR-MN can maintain normal blood glucose levels for at least 12 h. This suggests that the basal-meal combined insulin delivery system may have great potential for reducing the risk of hypoglycemia and improving daily continuous blood glucose control [4].

Measurement of plasma insulin in rats by the Elisa test further revealed the continuous supplementation of insulin under the treatment of EMNs [4]. The pharmacokinetic parameters (Fig. 8d) were analyzed, and the area under the curve value was comparable to that of insulin injection and insulin-loaded IR-MNs (Table S3). Subcutaneous injection caused a sharp increase in insulin, reaching a peak concentration at 1 h after treatment, and then significantly decreased to a negligible level within 4 h. On the other hand, in the case of XR-MN treatment, plasma insulin concentration fluctuated between 6 and 15 μIU/mL at T_{max}. These results confirmed that insulin administered by EMN was almost completely absorbed from the skin to the systemic circulation, and the biological activity of the released insulin remained intact after exposure to MN matrix materials. This indicates that EMN can not only prolong blood glucose control but also effectively reduce the risk of excessive fluctuations and hypoglycemia.

In summary, these results present further evidence supporting the higher drug loading capacity of one-step 3D printed EMN patches, which allows for a reduction in patch size while still meeting the daily insulin requirements of the human body. Furthermore, these patches can effectively address both post-prandial and basal insulin needs by employing diverse release strategies. In addition, the utilization of low-cost PDES as the 3D printing ink enables the fabrication of an insulin-loaded EMN patch for <1 US cent (Table S4). Notably, this cost is significantly lower than conventional insulin injections, eliminating the need for any additional therapeutic device. As a result, this innovative method offers a more affordable and accessible treatment option, effectively addressing a major challenge faced by diabetes patients worldwide.

3. Conclusions

Microneedle patches offer a promising and effective smart sensor and drug administration system, but current fabrication methods including negative molding and 3D printing techniques suffer from limitations such as inadequate drug encapsulation, high cost, and time-consuming processes. In this study, we present a novel approach for the fast multi-material 3D printing of multi-functional EMN patches. The designed multi-material EMNs exhibit high conductive, excellent mechanical strength, biocompatibility, and tunable drug release kinetics, making them suitable for wearable monitoring and transdermal drug delivery applications. Compared to the current 3D printing MNs inks [17–21], the low-cost PDES used in this study allows for fast and efficient photopolymerization, facilitating the fabrication of high-precision (MN tip diameter < 20 μm) MN patches within 20 min. In addition, PDES has high drug solubility, with ibuprofen being approximately 18,215 times more soluble in PDES compared to water—a feature absents in existing 3D printing MNs inks. Additionally, PDES allows for customization of drug release profiles by controlling the content of porogen and crosslinker. More importantly, when combined with the multi-material hierarchical 3D printing technique, PDES enables the creation of MN patches with tailored structures and functionalities. The ability to design and produce personalized MNs that cater to individual needs, coupled with the rapid printing process, signifies a transformative step towards personalized medicine.

As a proof-of-concept, three kinds of multi-material EMNs with different functions have been 3D printed. Wearable wireless EMNs monitor offer real-time and accurate detection of body movements, which benefit in joint disease diagnosis and wound healing. In the realm of glucose detection, the colorimetric EMNs provide a painless and efficient alternative to traditional glucometers. Different from the reported skin ISF detection MNs system, the developed EMN-based colorimetric sensor is considered to be a multifunctional gel with promising applications in smart biosensors. In addition, the drug-loaded EMN's capability for tunable drug delivery offering both immediate and extended-release options showcased the potential to revolutionize diabetes management.

This achievement provides a potential smart sensor and drug administration, improves the quality of life for diabetic or chronic patients worldwide. Diabetes mellitus is a chronic disease with high morbidity and frequent complications, bringing heavy social and economic burdens every year. The generation of multi-functional EMN brings good news to billions of diabetic patients worldwide, as they will no longer have to suffer from the pain of repeated penetrations for diagnosis or treatment. All they have to do is apply multi-functional EMNs regularly as instructed or recommended by doctors, which is both simple and convenient. Due to the safe and non-invasive nature of microneedle technology, the skin tissues will recover quickly and will not be harmed even after being penetrated by these EMNs multiple times. Besides, the use of these devices is economical. The material cost of a single EMN is approximately 1 US cent. In addition to insulin, the proposed EMNs are expected to load and deliver other bioactive substances (*e.g.*, growth factors, exosomes, drug-carrying nanoparticles, *etc.*) for the treatment of various diseases. Overall, the fast multi-material 3D printing and high drug-loading capabilities of EMNs address the limitations of conventional MN preparation methods, paving the way for the development of multi-functional MN patches for personalized medicine applications.

4. Methods

4.1. Materials

Choline chloride (ChCl), 2-Hydroxyethyl methacrylate (HEMA), itaconic acid (IA), poly (ethylene glycol) diacrylate (PEGDA), glycerol (Gly), ethyl phenyl (2,4,6-trimethylbenzoyl) phosphinate (TPO-L), polyethylene glycol (PEG) 1500, poly(ethylene glycol) diacrylate (PEGDA, the molecular weight = 400) and acetonitrile were purchased from Aladdin Bio-Chem Tech Co., Ltd. (Shanghai, China). Horseradish peroxidase (HRP), Glucose oxidase (Gox) enzyme, 3,3′,5,5'-Tetramethylbenzidine (TMB) and Insulin were purchased from J&K Scientific (Beijing, China). The Keygen Biotech Co., Ltd. (Nanjing, China) supplied the enzyme-linked immunosorbent assay (ELISA) detection kit. All other chemical reagents were obtained from Sinopharm Chemical Reagent Co., Ltd. (Beijing, China). Unless otherwise stated, ultrapure water from a reverse osmosis membrane system was used for aqueous solutions.

Kunming (KM) mice (25 ± 2 g) and Sprague Dawley (SD) rats (280 ± 20 g) were provided by SPF Biotech Co., Ltd. (Beijing, China). All animals were treated following the Laboratory Animal Care and Use Guidelines strictly. The protocols were reviewed and approved by the Institutional Animal Care and Use Committee of the Beijing Institute of Technology (approval number: BIT-EC-0010-M-036).

4.2. Preparation of PDES

Based on the polymerizable PDES prescription formulation design, the drug-loaded MN needle portion and the backing layer of the MN were designed as rigid and stretchable eutectogels, respectively. Two

types of eutectogel were created using ChCl as the hydrogen bond acceptor. For the rigid eutectogel, HEMA and IA were utilized as hydrogen bond donors, and PEG1500, a functional hydrogen bond acceptor, was added to enhance drug release performance. On the other hand, the flexible stretchable eutectogel was created using HEMA and glycerol as hydrogen bond donors. Homogeneous liquids were prepared by mixing the hydrogen bond acceptor and hydrogen bond donor in specific molar ratios (Table S1) in glass vessels and heating them (80 °C) while stirring on a magnetic stirrer for 20 min. The prepared PDES were further added with crosslinker, photoinitiator and APIs to formulate the 3D printing ink.

4.3. The effect of PDES on the solubility and stability of drugs

To ascertain the drug's solubility in DES, surplus drug was incorporated into the PDES, and agitated vigorously until the excess solid became insoluble. The solution obtained, which contained an excess of the drug, was left to stand for 24 h to achieve equilibrium. Prior to measuring solubility, solutions containing an excess of the drug were passed through a syringe filter unit with a 0.22 μm membrane. Then, the samples of the liquid were diluted in super pure water, and the contents of the drugs were tested by a U*V* spectrometer (PG instruments) using calibration curves.

To assess the stability of insulin in EMNs, a eutectogel containing 2 mg/g of insulin was prepared and refrigerated at 4 °C. Subsequently, the sample was extracted with 20 times the weight of PBS solution through ultrasonic extraction for 30 min. The insulin content was accurately analyzed through HPLC utilizing a C18 chromatographic column (5 μm, 4.6 × 150 mm, Nanochrom Tech Co., Ltd) at 214 nm [67]. The mobile phase consisted of 0.2 mol/L sulfate buffer and acetonitrile (74:26 (*V*/V)) at a flow rate of 1 mL/min. Each sample was loaded three times, and the average readings were obtained for further quantification. To further evaluate the stability of the secondary structure of insulin, the circular dichroism analysis of insulin between 20 °C, 190 and 260 nm before and after preparation was recorded through a circular dichroism spectrometer (J-1500, Jasco, Japan).

4.4. Photopolymerization of PDES

Crosslinker PEGDA (0.1% *w*/w) and photoinitiator TPO-L (0.1% w/w) were added to the DES, and the precursor solution was stirred at room temperature until a homogeneous, colorless solution was produced. The precursor solution was then injected into two silicone films with a thickness of 1 mm. The UV light source (RW-UVA, Anycubic, China) was then used to initiate the reaction by exposing it to a primary wavelength of 405 nm.

The resulting eutectogel was immersed in methanol twenty times and subjected to ultrasonic oscillation (KQ-300DE, Keqiao Equipment Co., Ltd., China) for 30 min. The supernatant was filtered through a 0.22 μm filter membrane, and the content of HEMA and IA was determined using HPLC [66]. The analysis was performed using a C18 chromatographic column (5 μm, 4.6 × 150 mm, Nanochrom Tech Co., Ltd.) at 210 nm. The mobile phase was a mixture of 0.1% phosphoric acid water and methanol in a ratio of 90: 10 (V/V), and the flow rate was 1 mL/min. Each sample was analyzed in triplicate, and the average readings were used for further quantification. The degree of polymerization of the eutectogel was determined by measuring the residual monomer content.

4.5. Characterization of eutectogel

The Nicolet Is-10 spectrometer was utilized to record Total Reflection Fourier Transform Infrared (ATR-FTIR) spectra within the wavenumber range of 400–4000 cm-1. Thermogravimetric analysis (TGA) was conducted using a Q50 thermogravimetric analyzer (TA, USA) in a nitrogen atmosphere, with a heating rate of 10 °C over a temperature range of 20–700 °C. The TGA was measured in a nitrogen atmosphere with a heating rate of 10 °C. Differential Scanning Calorimetry (DSC) was performed using a DSC-60 tester (Shimadzu, Japan). The mixture was heated at a rate of 10 °C/min in a nitrogen atmosphere from −50 °C to 150 °C in an aluminum pan. X-ray diffraction (XRD-6000, Shimadzu, Japan) was used to analyze the amorphous phase of DES. The scanning speed was 2°/min within the range of 5° ~ 80°, under the condition of CuKa (emission wavelength 0.15406) ray with a tube current of 40 mA and tube voltage of 40 kV. To determine the conductivity of the eutectogel, electrochemical characterization was performed using a CHI660E electrochemical workstation (Chen Hua Instruments, China).

4.6. 3D printing EMNs

The production of MNs is achieved through the utilization of a bottom-up DLP 3D printing device (Photon Ultra, Anycubic, China) operating at a UV–visible wavelength of 405 nm. A customized model is created using TinkerCAD software for the digital printing process. The slicing function employs the Photon Workshop software for continuous image projection. The MN backing layer is printed at a single layer height of 1 mm, with each layer being cured for 30–60 s. The MN needle portion is printed at a single layer height of 0.05 mm, with each layer being cured for 2–30 s. After 3D printing, the EMNs were then cured in a UV post-cure chamber (3.3 mW/cm^2 light intensity) for 10 min and then soaked the EMNs in 70%*v*/v ethanol for 30 s, followed by water for 30 s to remove monomers that were not fully polymerized.

4.7. Characterization of MN patches

In this study, the vertical microscope (4800-B, Tontruth, China) and scanning electron microscope (SEM) (JSM-7500F, Shimadzu, Japan) were utilized. Before SEM analysis, samples were freeze-dried and coated with gold. The mechanical properties of EMNs were evaluated using a universal testing machine (AGS-J, Shimadzu, Japan). The MN elastic backing layer was stretched at a speed of 3 mm/min, while force and displacement were continuously measured. The compression test involved measuring the fracture and penetration forces of the MN. To determine the breaking force, MNs were placed between metal parallel plates and compressed vertically at a speed of 1 mm/s until fracture or deformation was detected. To determine the piercing force, MNs were placed above metal parallel plates with porcine cadaver skin below, compressed vertically at a speed of 1 mm/s, and the stress-strain curve resulting from the MN insertion behavior was detected.

4.8. Finite element analysis

The behavior of MNs during mechanical strength testing and insertion into the skin was simulated using the finite element analysis software Abaqus 6.1. The MN body's actual material mechanics characterization (refer to Table S5) was utilized, while the structure and parameters of the skin (refer to Table S6) were set based on literature reports [68–70]. The 3D model of the MN and skin structure was meshed using hexahedral elements. The insertion process was executed using a static conventional step with an incremental period of 60 s, and the initial increment of each iteration was 0.5 s. The simulation of different MNs' breaking force (refer to Fig. 4a) and penetration force (refer to Fig. 4b) was conducted. Finally, a specific needle shape's finite element simulation results were validated through corresponding experiments.

4.9. MN piercing skin performance

The manufactured MNs were inserted into the separated porcine skin with the thickness of 1.62 ± 0.27 mm to evaluate their efficacy. Puncture marks on the skin surface were examined under a bright field microscope to determine the insertion rate after insertion. Skin samples were collected from the middle of the pinhole for histological analysis using HE staining and sectioning. To observe the drug distribution at

different depths, Confocal Laser Scanning Microscopy (CLSM) was used for *in vivo* skin insertion studies. The MN was loaded with RhB in eutectogel. Mice were anesthetized and the MN was inserted into the back skin for 10 min. After euthanizing the mice, the administration site was excised and placed on a cover glass for CLSM imaging using STELLARIS (Leica, Germany). The imaging plane was defined as the skin surface (z = 0 μm).

4.10. Biocompatibility of MNs

The cytotoxicity of EMNs on NIH-3 T3 fibroblast cells was assessed using live-dead cell staining and CCK-8 assay. Initially, a 96-well plate was seeded with NIH-3 T3 fibroblast cells (5000 cells per well) and incubated for 24 h until cell adhesion. Subsequently, the plate was placed in a humidified incubator (37 °C, 5% CO2) and treated with a continuous dilution of the MN solution, which was dissolved in 1 mg/mL. After 72 h of incubation, the cells were stained using a calcein AM/PI double staining kit (Keygen Biotech, China) and observed under a microscope.

To further demonstrate the biocompatibility of EMN, various concentrations of MN extract were added to the cells. The MN extracts were obtained by adding 3D printed EMN to the medium solution, followed by co-culturing at 37 °C for 48 h. After 24 h of incubation, the medium was replaced with fresh medium containing CCK-8 reagent (0.1 mL) and incubated for 2 h. The relative cell survival percentage was determined by calculating the final absorbance at 450 nm using a microplate reader (Imark, BIORAD, USA). Cells cultured in the initial medium served as negative controls.

To evaluate the skin and tissue response following MN application, EMN was applied to the depilated back skin of mice, removed after 10 min, and the application site was photographed using a digital camera. The same procedure was performed on human volunteers to record any irritation, such as erythema, bleeding, or edema.

4.11. Fabrication and testing of EMN motion monitoring sensor

To explore the potential of EMN in the field of flexible sensors, a wireless monitor using EMN was developed. The EMN was attached to the skin of volunteers, and the two ends of the EMN were connected to the electrodes of the monitor. A Mechanical strain was applied to EMN and the resistance variations were recorded by the monitor and transmitted to a smartphone *via* Bluetooth. To quantitatively assess the sensing property, the resistance change rate was $\Delta R/R_0 \times 100$, where R_0 is the initial resistance in an unaltered state, and ΔR is the difference between resistance in the deformed state and R_0.

4.12. Fabrication of the colorimetric EMN for glucose detection

Colorimetric EMNs (CEMNs) were prepared using a method building upon prior work with 3D printing multi-material EMNs. This involved adding 0.04 mg/mL of HRP and 10 mg/mL of GOx enzyme to PDES. After 3D printing, the backing layer was immersed in a 4 mg/mL TMB solution for 10 min and air-dried. The EMNs were applied to mice's backs for 10 min, and pre- and post-application weights were recorded to calculate skin ISF extraction weight per patch. To evaluate its fluid extraction and glucose detection capacity, 1% agarose gels with varying glucose concentrations were prepared. CEMNs were applied to these agarose gels for 10 min. Images of CEMNs were captured using a smartphone equipped with a custom app to calculate RGB values in the central patch area. For on-skin blood glucose level (BGL) detection, animal experiments were conducted on STZ-induced diabetic mice. Initially, tail vein blood was collected to determine baseline BGL using a blood glucose meter (I-580, Yuyue Medical Equipment Co., Ltd., China). CEMNs were then applied to the mice for 10 min, and color changes were recorded with a smartphone. Subsequently, red, green, and blue values were obtained using a custom app. BGLs of the STZ-induced diabetic mice were determined by comparing recorded RGB values to respective calibration curves developed for on-skin BGL monitoring.

4.13. Drug release behavior of EMN in vivo and in vitro

For the penetration test, fresh porcine skin was obtained from the market. The *in vitro* insulin release experiment was conducted by piercing insulin-loaded MNs with varying PEG1500 contents (% relative to PDES) into the porcine cadaver skin and detecting the insulin content in the receiving solution. One piece of EMNs patch (1 cm^2,10 × 10) contain only a needle portion weighing 0.03 g. Type I diabetic patients require approximately 16 IU of insulin per day [52]. Therefore, the insulin content of PDES used for the *in vitro* release experiments was 33 mg/g to ensure that each EMNs patch contained 1 mg (about 26 IU) of insulin. Specifically, the MN was attached to isolated porcine cadaver skin using a modified Franz diffusion cell. The receiving solution, a 0.1 M PBS solution, was continuously stirred at 200 rpm and maintained at 37 °C throughout the analysis. To determine the insulin release of the prepared MN, 500 μL of the sample was taken at a predetermined time point and an equal volume of fresh receiving solution was added. The actual concentration of insulin in each obtained sample was quantified using HPLC. To further characterize the diffusion release behavior of the MN, a MN patch loaded with fluorescein sodium was prepared and applied to mice. The *in vivo* imaging system (IVIS) (Xenogen 200, Caliper Life Sciences, USA) was used to measure the fluorescence intensity and determine the *in vivo* drug delivery efficiency.

4.14. Diabetes animal model and MNs treatment

The laboratory animals were acclimatized to standard conditions for over two weeks before any experimentation. Diabetic mice were induced by intraperitoneal injection of STZ (100 mg/kg body weight) dissolved in 0.2 mL of sodium citrate buffer solution (pH 4.5, 0.05 M) after an overnight fast. Blood glucose levels of the treated mice were monitored for one week using a blood glucose meter (I-580, Yuyue Medical Equipment Co., Ltd., China) until they stabilized. Only mice with blood glucose levels exceeding 11.1 mM were considered diabetic and used in this study. The content of insulin in PDES is 0.063 μg/g to make sure each EMN patch used in each mouse contains 50 μIU of insulin. Before the experiment, diabetic mice were anesthetized with 2% isoflurane gas, and their hind hair was gently shaved. The insulin-loaded MN patch (50 μIU) was then inserted into the dorsal skin and secured with surgical tape. As a control experiment, the same dose of insulin solution was subcutaneously injected. Blood samples were collected from the cutting tip of the tail at selected time points (0 to 12 h) after treatment, and the relationship between blood glucose levels and time was measured using a blood glucose meter. The pharmacokinetic behavior of insulin in animals was determined by piercing the insulin-loaded MN into the skin of healthy rats. The collected blood samples were centrifuged at 3000 rpm for 10 min to obtain plasma, which was then frozen and stored at −20 °C until analyzed using an insulin ELISA kit to measure the plasma levels of insulin delivered to the rats.

4.15. Statistical analysis

All analyses were conducted using a minimum sample size of $n \geq 3$. Data analysis was performed using Excel and Origin 9. Descriptive statistics were presented as mean ± SE. The *t*-test was employed to compare data points. A statistical difference was considered repeatable when $P < 0.05$. Significance is denoted in the figures as $^*P < 0.05$, $^{**}P < 0.01$, $^{***}P < 0.001$.

Supplementary data to this article can be found online at https://doi.org/10.1016/j.jconrel.2024.02.023.

CRediT authorship contribution statement

Xinmeng Zhou: Data curation. **Aminov Nail:** Writing – review & editing, Investigation. **Hao Yu:** Methodology. **Zilian Yu:** Software. **Yue Sun:** Writing – original draft. **Kun Wang:** Project administration. **Nanbin Bao:** Methodology. **Decheng Meng:** Writing – original draft. **Liran Zhu:** Formal analysis. **Huanjun Li:** Writing – original draft, Conceptualization.

Declaration of competing interest

The authors declare no conflict of interest.

Data availability

Data will be made available on request.

Acknowledgements

We thank the Analysis and Testing Center at the Beijing Institute of Technology and all our partners for their efforts and help. This work was jointly supported by the National Natural Science Foundation of China (21736001, 21174017) and, Basalt Fiber Research Project of the Beijing Institute of Technology (2021XW005).

References

[1] B.Z. Chen, Y.T. He, Z.Q. Zhao, Y.H. Feng, L. Liang, J. Peng, C.Y. Yang, H. Uyama, M.-A. Shahbazi, X.D. Guo, Strategies to develop polymeric microneedles for controlled drug release, Adv. Drug Deliv. Rev. 5 (2023) 115109.
[2] B.Z. Chen, L.Q. Zhang, Y.Y. Xia, X.P. Zhang, X.D. Guo, A basal-bolus insulin regimen integrated microneedle patch for intraday postprandial glucose control, Sci. Adv. 6 (2020) eaba7260.
[3] C. Yang, T. Sheng, W. Hou, J. Zhang, L. Cheng, H. Wang, W. Liu, S. Wang, X. Yu, Y. Zhang, J. Yu, Z. Gu, Glucose-responsive microneedle patch for closed-loop dual-hormone delivery in mice and pigs, Sci. Adv. 8 (2022) eadd3197.
[4] K. Ita, Transdermal delivery of drugs with microneedles-potential and challenges, Pharmaceutics 7 (2015) 90–105.
[5] X. Chen, L. Wang, H. Yu, C. Li, J. Feng, F. Haq, A. Khan, R.U. Khan, Preparation, properties and challenges of the microneedles-based insulin delivery system, J. Control. Release 288 (2018) 173–188.
[6] U. Detamornrat, E. McAlister, A.R.J. Hutton, E. Larraneta, R.F. Donnelly, The role of 3d printing technology in microengineering of microneedles, Small 18 (2022) 2106392.
[7] Z. Luo, Y. Wang, J. Li, J. Wang, Y. Yu, Y. Zhao, Tailoring hyaluronic acid hydrogels for biomedical applications, Adv. Funct. Mater. 2306554 (2023).
[8] R. Wang, G. Jiang, U.E. Aharodnikau, K. Yunusov, Y. Sun, T. Liu, S.O. Solomevich, Recent advances in polymer microneedles for drug transdermal delivery: design strategies and applications, Macromol. Rapid Commun. 43 (2022) 2200037.
[9] J. Yang, J. Yang, X. Gong, Y. Zheng, S. Yi, Y. Cheng, Y. Li, B. Liu, X. Xie, C. Yi, L. Jiang, Recent progress in microneedles-mediated diagnosis, therapy, and theranostic systems, Adv. Healthc. Mater. 11 (2022) 2102547.
[10] W. Yao, D. Li, Y. Zhao, Z. Zhan, G. Jin, H. Liang, R. Yang, 3D printed multi-functional hydrogel microneedles based on high-precision digital light processing, Micromachines 11 (2020) 17–28.
[11] S.H. Lim, W.J. Tiew, J. Zhang, P.C.-L. Ho, N.N. Kachouie, L. Kang, Geometrical optimisation of a personalised microneedle eye patch for transdermal delivery of anti-wrinkle small peptide, Biofabrication 12 (2020) 035003.
[12] A.R. Johnson, C.L. Caudill, J.R. Tumbleston, C.J. Bloomquist, K.A. Moga, A. Ermoshkin, D. Shirvanyants, S.J. Mecham, J.C. Luft, J.M. DeSimone, Single-step fabrication of computationally designed microneedles by continuous liquid interface production, PLoS One 11 (2016) e0162518.
[13] C.L. Caudill, J.L. Perry, S. Tian, J.C. Luft, J.M. DeSimone, Spatially controlled coating of continuous liquid interface production microneedles for transdermal protein delivery, J. Control. Release 284 (2018) 122–132.
[14] C. Caudill, J.L. Perry, K. Iliadis, A.T. Tessema, B.J. Lee, B.S. Mecham, S. Tian, J. M. DeSimone, Transdermal vaccination via 3D-printed microneedles induces potent humoral and cellular immunity, P. Nat. L. Acad. Sci. USA 118 (2021) e2102595118.
[15] N.U. Rajesh, I. Coates, M.M. Driskill, M.T. Dulay, K. Hsiao, D. Ilyin, G.B. Jacobson, J.W. Kwak, M. Lawrence, J. Perry, C.O. Shea, S. Tian, J.M. DeSimone, 3D-printed microarray patches for transdermal applications, JACS Au 2 (2022) 2426–2445.
[16] S.R. Dabbagh, M.R. Sarabi, R. Rahbarghazi, E. Sokullu, A.K. Yetisen, S. Tasoglu, 3D-printed microneedles in biomedical applications, iScience 24 (2021) 102012.
[17] L. Barnum, J. Quint, H. Derakhshandeh, M. Samandari, F. Aghabaglou, A. Farzin, L. Abbasi, S. Bencherif, A. Memic, P. Mostafalu, A. Tamayol, 3D-printed hydrogel-filled microneedle arrays, Adv. Healthc. Mater. 10 (2021) 2001922.
[18] S.H. Lim, H. Kathuria, M.H.B. Amir, X. Zhang, H.T.T. Duong, P.C.L. Ho, L. Kang, High resolution photopolymer for 3D printing of personalised microneedle for transdermal delivery of anti-wrinkle small peptide, J. Control. Release 329 (2021) 907–918.
[19] C.T. Hagan, C. Bloomquist, S. Warner, N.M. Knape, I. Kim, H. Foley, K.T. Wagner, S. Mecham, J. DeSimone, A.Z. Wang, 3D printed drug-loaded implantable devices for intraoperative treatment of cancer, J. Control. Release 344 (2022) 147–156.
[20] C.J. Bloomquist, M.B. Mecham, M.D. Paradzinsky, R. Januszewicz, S.B. Warner, J. C. Luft, S.J. Mecham, A.Z. Wang, J.M. DeSimone, Controlling release from 3D printed medical devices using CLIP and drug-loaded liquid resins, J. Control. Release 278 (2018) 9–23.
[21] C.T. Hagan, C. Bloomquist, I. Kim, N.M. Knape, J.D. Byrne, L. Tu, K. Wagner, S. Mecham, J. DeSimone, A.Z. Wang, Continuous liquid interface production of 3D printed drug-loaded spacers to improve prostate cancer brachytherapy treatment, Acta Biomater. 148 (2022) 163–170.
[22] S.N. Economidou, D. Douroumis, 3D printing as a transformative tool for microneedle systems: recent advances, manufacturing considerations and market potential, Adv. Drug Deliv. Rev. 173 (2021) 60–69.
[23] M. Tan, Y. Xu, Z. Gao, T. Yuan, Q. Liu, R. Yang, B. Zhang, L. Peng, Recent advances in intelligent wearable medical devices integrating biosensing and drug delivery, Adv. Mater. 34 (2022) 2108491.
[24] M.H. Zainal-Abidin, M. Hayyan, G.C. Ngoh, W.F. Wong, C.Y. Looi, Emerging frontiers of deep eutectic solvents in drug discovery and drug delivery systems, J. Control. Release 316 (2019) 168–195.
[25] Y. Guo, Y. Wang, H. Chen, W. Jiang, C. Zhu, S. Toufouki, S. Yao, A new deep eutectic solvent-agarose gel with hydroxylated fullerene as electrical "switch" system for drug release, Carbohydr. Polym. 296 (2022) 119939.
[26] C. Huang, X. Chen, C. Wei, H. Wang, H. Gao, Deep eutectic solvents as active pharmaceutical ingredient delivery systems in the treatment of metabolic related diseases, Front. Pharmacol. 12 (2021) 794939.
[27] Y. Cao, Y.J. Tan, S. Li, W.W. Lee, H. Guo, Y. Cai, C. Wang, B.C.K. Tee, Self-healing electronic skins for aquatic environments, Nat. Electron. 2 (2019) 75–82.
[28] R. Li, K. Zhang, G. Chen, B. Su, M. He, Stiff, self-healable, transparent polymers with synergetic hydrogen bonding interactions, Chem. Mater. 33 (2021) 5189–5196.
[29] G. de Araujo Lima, M.E. Di Pietro e Souza, V. Vanoli, W. Panzeri, F. Briatico-Vangosa, F. Castiglione, A. Mele, Hydrophobic eutectogels: a new outfit for non-ionic eutectic solvents, Mater. Today. Chem. 29 (2023) 101402.
[30] X. Zou, X. Wang, Z. Bai, O. Yue, C. Wei, L. Xie, H. Zhang, X. Liu, Environment-tolerant versatile ion-conductive eutectic hydrogels for self-powered wearable flexible sensors, Chem. Eng. J. 463 (2023) 142349.
[31] C. Zhang, H. Zheng, J. Sun, Y. Zhou, W. Xu, Y. Dai, J. Mo, Z. Wang, 3D printed, solid-state conductive ionoelastomer as a generic building block for tactile applications, Adv. Mater. 34 (2022) 2105996.
[32] L. Cai, G. Chen, J. Tian, B. Su, M. He, Three-dimensional printed ultrahighly sensitive bioinspired ionic skin based on submicrometer-scale structures by polymerization shrinkage, Chem. Mater. 33 (2021) 2072–2079.
[33] A. Sadeqi, G. Kiaee, W. Zeng, H. Rezaei Nejad, S. Sonkusale, Hard polymeric porous microneedles on stretchable substrate for transdermal drug delivery, Sci. Rep. 12 (2022) 1853.
[34] N.H. Khan, M. Mir, L. Qian, M. Baloch, M.F. Ali Khan, A.U. Rehman, E.E. Ngowi, D. D. Wu, X.Y. Ji, Skin cancer biology and barriers to treatment: recent applications of polymeric micro/nanostructures, J. Adv. Res. 36 (2022) 223–247.
[35] B. Weidinger, G. Yang, N. von Coelln, H. Nirschl, I. Wacker, P. Tegeder, R. R. Schröder, E. Blasco, 3D printing hierarchically nano-ordered structures, Adv. Sci. 10 (2023) 2107643.
[36] M. Kasprow, D. Lipowska-Kur, L. Otulakowski, A. Dworak, B. Trzebicka, HEMA in polymers with thermoresponsive properties, Polym. Rev. 61 (2021) 714–735.
[37] S. Haddadzadegan, F. Dorkoosh, A. Bernkop-Schnürch, Oral delivery of therapeutic peptides and proteins: technology landscape of lipid-based nanocarriers, Adv. Drug Deliv. Rev. 182 (2022) 114097.
[38] J. Zhu, Y. Wei, J. Zhang, S. Qian, Y. Gao, W. Heng, Are all poorly soluble drugs dissolved in deep eutectic solvents true solutions? J. Colloid Interface Sci. 645 (2023) 813–822.
[39] H. Wei, S. Liu, Z. Tong, T. Chen, M. Yang, Y. Guo, H. Sun, Y. Wu, Y. Chu, L. Fan, Hydrogel-based microneedles of chitosan derivatives for drug delivery, React. Funct. Polym. 172 (2022) 105200.
[40] K. Yu, X. Zhang, Y. Sun, Q. Gao, J. Fu, X. Cai, Y. He, Printability during projection-based 3D bioprinting, Bioact. Mater. 11 (2022) 254–267.
[41] J.R. Elmore, G.N. Dexter, D. Salvachua, J. Martinez-Baird, E.A. Hatmaker, J. D. Huenemann, D.M. Klingeman, G.L. Peabody, D.J. Peterson, C. Singer, G. T. Beckham, A.M. Guss, Production of itaconic acid from alkali pretreated lignin by dynamic two stage bioconversion, Nat. Commum 12 (2021) 2261.
[42] B.-E. Teleky, D.C. Vodnar, Biomass-derived production of itaconic acid as a building block in specialty polymers, Polymers 11 (2019) 1035.
[43] J. Yang, H. Zhang, T. Hu, C. Xu, L. Jiang, Y. Shrike Zhang, M. Xie, Recent advances of microneedles used towards stimuli-responsive drug delivery, disease theranostics, and bioinspired applications, Chem. Eng. J. 426 (2021) 130561.
[44] Q. Yan, S. Shen, Y. Wang, J. Weng, A. Wan, G. Yang, L. Feng, The finite element analysis research on microneedle design strategy and transdermal drug delivery system, Pharmaceutics 14 (2022) 1625.
[45] M. Ali, S. Namjoshi, H.A.E. Benson, Y. Mohammed, T. Kumeria, Dissolvable polymer microneedles for drug delivery and diagnostics, J. Control. Release 347 (2022) 561–589.
[46] J.D. Mota-Morales, M.C. Gutiérrez, M.L. Ferrer, R. Jiménez, P. Santiago, I. C. Sanchez, M. Terrones, F. Del Monte, G.J.J.o.M.C.A. Luna-Bárcenas, Synthesis of

macroporous poly (acrylic acid)–carbon nanotube composites by frontal polymerization in deep-eutectic solvents, J. Mater. Chem. A 1 (2013) 3970–3976.
[47] G.D. Mogoşanu, A.M.J.I.j.o.p. Grumezescu, Natural and synthetic polymers for wounds and burns dressing, Int. J. Pharm. 463 (2014) 127–136.
[48] S. Roig-Sanchez, D. Kam, N. Malandain, E. Sachyani-Keneth, O. Shoseyov, S. Magdassi, A. Laromaine, A. Roig, One-step double network hydrogels of photocurable monomers and bacterial cellulose fibers, Carbohydr. Polym. 294 (2022) 119778.
[49] M. Tan, Y. Xu, Z. Gao, T. Yuan, Q. Liu, R. Yang, B. Zhang, L. Peng, Recent advances in intelligent wearable medical devices integrating biosensing and drug delivery, Adv. Mater. 34 (2022) 2108491.
[50] X. Jin, D.D. Zhu, B.Z. Chen, M. Ashfaq, X.D. Guo, Insulin delivery systems combined with microneedle technology, Adv. Drug Deliv. Rev. 127 (2018) 119–137.
[51] S.B. Catrina, K. Okamoto, T. Pereira, K. Brismar, L. Poellinger, Hyperglycemia regulates hypoxia-inducible factor-1α protein stability and function, Diabetes 53 (2004) 3226–3232.
[52] A. Elsayed, M. Al-Remawi, N. Jaber, K.M. Abu-Salah, Advances in buccal and oral delivery of insulin, Int. J. Pharm. 633 (2023) 51–70.
[53] Y. Yang, R. Zhou, Y. Wang, Y. Zhang, J. Yu, Z. Gu, Recent advances in oral and transdermal protein delivery systems, Angew. Chem. Int. Ed. 62 (2023) e202214795.
[54] S. Ross, N. Scoutaris, D. Lamprou, D. Mallinson, D. Douroumis, Inkjet printing of insulin microneedles for transdermal delivery, Drug. Deliv. Transl. Re. 5 (2015) 451–461.
[55] M. Wu, Y. Zhang, H. Huang, J. Li, H. Liu, Z. Guo, L. Xue, S. Liu, Y. Lei, Assisted 3D printing of microneedle patches for minimally invasive glucose control in diabetes, Mater. Sci. Eng. C 117 (2020) 111299.
[56] S.N. Economidou, C.P. Pissinato Pere, M. Okereke, D. Douroumis, Optimisation of design and manufacturing parameters of 3d printed solid microneedles for improved strength, sharpness, and drug delivery, Micromachines 12 (2021) 1–16.
[57] C.P.P. Pere, S.N. Economidou, G. Lall, C. Ziraud, J.S. Boateng, B.D. Alexander, D. A. Lamprou, D. Douroumis, 3D printed microneedles for insulin skin delivery, Int. J. Pharm. 544 (2018) 425–432.
[58] S.N. Economidou, C.P.P. Pere, A. Reid, M.J. Uddin, J.F.C. Windmill, D.A. Lamprou, D. Douroumis, 3D printed microneedle patches using stereolithography (SLA)for intradermal insulin delivery, Mater. Sci. Eng. C 102 (2019) 743–755.
[59] J. Yu, Y. Zhang, Y. Ye, R. DiSanto, W. Sun, D. Ranson, F.S. Ligler, J.B. Buse, Z. Gu, Microneedle-array patches loaded with hypoxia-sensitive vesicles provide fast glucose-responsive insulin delivery, Diabet. Technol. Therapeut. 18 (2016) S54–S55.
[60] D.D. Zhu, X.P. Zhang, C.B. Shen, Y. Cui, X.D. Guo, The maximum possible amount of drug in rapidly separating microneedles, Drug. Deliv. Transl. Re. 9 (2019) 1133–1142.
[61] Y. Ito, M. Hirono, K. Fukushima, N. Sugioka, K. Takada, Two-layered dissolving microneedles formulated with intermediate-acting insulin, Int. J. Pharm. 436 (2012) 387–393.
[62] K.Y. Seong, M.S. Seo, D.Y. Hwang, E.D. O'Cearbhaill, S. Sreenan, J.M. Karp, S. Y. Yang, A self-adherent, bullet-shaped microneedle patch for controlled transdermal delivery of insulin, J. Control. Release 265 (2017) 48–56.
[63] J. Yu, J. Wang, Y. Zhang, G. Chen, W. Mao, Y. Ye, A.R. Kahkoska, J.B. Buse, R. Langer, Z. Gu, Glucose-responsive insulin patch for the regulation of blood glucose in mice and minipigs, Nat. Biomed. Eng. 4 (2020) 499–506.
[64] J.D. Kim, M. Kim, H. Yang, K. Lee, H. Jung, Droplet-born air blowing: novel dissolving microneedle fabrication, J. Control. Release 170 (2013) 430–436.
[65] X. Li, X. Huang, J. Mo, H. Wang, Q. Huang, C. Yang, T. Zhang, H.J. Chen, T. Hang, F. Liu, L. Jiang, Q. Wu, H. Li, N. Hu, X. Xie, A fully integrated closed-loop system based on mesoporous microneedles-iontophoresis for diabetes treatment, Adv. Sci. 8 (2021) e2100827.
[66] L. Yin, X. Zhao, L. Cui, J. Ding, M. He, C. Tang, C. Yin, Cytotoxicity and genotoxicity of superporous hydrogel containing interpenetrating polymer networks, Food Chem. Toxicol. 47 (2009) 1139–1145.
[67] A. Najjar, M. Alawi, N. AbuHeshmeh, A.J.A.i.P. Sallam, A rapid, isocratic HPLC method for determination of insulin and its degradation product, Adv. Pharmacol. Sci. 2014 (2014) 58–65.
[68] B. Newell, W. Zhan, Mathematical modelling of microneedle-mediated transdermal delivery of drug nanocarriers into skin tissue and circulatory system, J. Control. Release 360 (2023) 447–467.
[69] F. Henriquez, D. Celentano, M. Vega, G. Pincheira, J.O. Morales, Modeling of microneedle arrays in transdermal drug delivery applications, Pharmaceutics 15 (2023) 358.
[70] F. Henriquez, J.O. Morales-Ferreiro, D. Celentano, Structural evaluation by the finite-element method of hollow microneedle geometries for drug delivery, Adv. Eng. Mater. 24 (2022) 2200049.